Development of WARES, a Wideband FPGA based Spectrometer for SEQUOIA

by

Sandra Guadalupe Bustamante González

Thesis submitted as a partial requirement for the degree of

Master of Science in Astrophysics

at the

Instituto Nacional de Astrofísica, Óptica y Electrónica

Febrero 2018

Tonantzintla, Puebla

Supervised by

Dr. Edgar Castillo Domínguez, INAOE
Dr. Gopal Narayanan, UMass
Dr. Arturo Gómez Ruiz, INAOE

Master of Science in Astrophysics

Development of a Wideband FPGA Spectrometer for SEQUOIA

by Sandra Bᴜꜱᴛᴀᴍᴀɴᴛᴇ

Abstract

SEQUOIA is a 16-pixel focal plane array for observation in the 3mm band and was first installed in the 14-m FCRAO telescope where it was responsible for the creation of the largest and most sensitive map for the Taurus Molecular Cloud and also, of the Galactic Ring Survey. Now, it is considered one of the first light instruments for LMT to be install by the end of 2017. In preparation for the installation, a new reconfigurable and expandable back-end for SEQUOIA was created. The back-end is a FPGA based polyphase filter bank spectrometer based on a ROACH 2 Board developed by CASPER. This thesis will first describe the hardware and software used . On Chapter 2, the hardware, and software tools used are described. The main components are ROACH 2 Board and ADC1x5000 ADC card. WARES will work on 3 operation modes: 800 MHz, 400 MHz, and 200 MHz. The FPGA designs and the differences between them are explained on Chapter 3. The characterization procedure was done in 3 steps described on Chapter 4. First, the ADC characterization resulted in the following parameters: SFDR$= 20$, SINAD$=$, and ENOB$=$. Second, the dynamic range was determined to be ≈ 20 dB. Third, Allan time obtained > 100 s. Additionally, test with SEQUOIA was included on Chapter 5 from which the receiver temperature was calculated to be $60 - 80$ K and have an consistent Allan time > 100 s. Finally, Chapter 6 includes a section of future work needed before the commissioning on the LMT.

INSTITUTO NACIONAL DE ASTROFISICA, OPTICA Y ELECTRONICA

Maestría en Ciencias en Astrofísica

Development of a Wideband FPGA Spectrometer for SEQUOIA

por Sandra BUSTAMANTE

Resumen

SEQUOIA es una cámara heterodina de plano focal de 16 pixeles para la observación en la banda de 3mm. SEQUOIA será instalada a finales del 2017 en el GTM. A pesar de haber operado en el 14m del FCRAO, son necesarias algunas modificaciones. Una de estas actualizaciones es WARES, un espectrómetro FPGA desarrollado con la tecnología de CASPER. En el Capítulo 2, se describe tanto el hardware y software utilizado para el desarrollo de WARES. Las principales componentes son una tarjeta de procesamiento ROACH 2 y dos tarjetas de adquisición de datos ADC1x5000. WARES tiene 3 modos de operacion segun la banda deseada: 800 MHz, 400 MHz, and 200 MHz. El código utilizado para estos modos es descrito en el Capítulo 3. El proceso de caracterización realizado en 3 pasos es descrito en el Capítulo 4. Durante el primer paso, se realizó la caracerización del ADC obteniendo los siguientes parámetros SFDR$= 20$, SINAD$=$, and ENOB$=$. El segundo paso, fue calcular el rango lineal, el cual fue determinado de ≈ 20 dB. El tercer paso, se encontró un tiempo de Allan > 100 s. Además en el Capítulo 5 se explica el proceso de cómo se determinó la temperatura del instrumento de $60 - 80$ K y un tiempo de Allan > 100 s utilizando SEQUOIA y WARES. Para finalizar en el Capítulo 6 se incluyen más actividades pendientes antes de realizar la instalación en el GTM.

Contents

List of Figures

List of Tables

Chapter 1

Introduction

Radio astronomy has proven to be an important field of study with numerous major discoveries, such as the discovery of interstellar molecules and its connection with star formation. These topics are relevant to the work currently being conducted at the LMT, a 50 m single dish radio telescope. The LMT is equipped with different instruments specialized in specific bands of the radio spectrum; among them is SEQUOIA, a 16 pixel heterodyne instrument that works in the 3 mm band. To increase the bandwidth of SEQUOIA, a wide-band FPGA-based spectrometer was developed. All of these topics will be further explained in this chapter.

1.1   Atmospheric Windows

The atmosphere absorbs most electromagnetic radiation, except in optical, infrared and radio wavelengths. This property of the earth's atmosphere allowed the first astronomical observations to be made in the optical range. Later on, the discovery of radio frequencies and the eventual detection of extraterrestrial radio noise led to the development of radio astronomy. The radio window extends from λ= 0.3 mm, which is the limit of the atmosphere opacity and far infrared, to 30 m, where the ionosphere starts to act as a mirror (Condon and Ransom, 2015.). In radio astronomy, these limits are more often represented as their corresponding frequency values of 1THz and 10MHz.

The radio window is not perfectly transparent but has sub-windows in which the atmosphere is nearly transparent. These windows are called atmospheric windows and are named after the central wavelength in the range. At millimeter wavelengths, there exist 3 atmospheric windows: 3 mm band that goes from 65 GHz to 115 GHz, 2 mm from 125 GHz to 180 GHz, and 1.2 mm from 200 GHz to 300 GHz. Many instruments in radio are design to *see* inside these windows. Figure 1.2 shows the simulated sky transmission at different frequencies at the LMT site, Sierra Negra. SEcond QUabbin Optical Imaging Array (SEQUOIA), the main instrument in this thesis which is later described, is designed to work in the 3mm band.
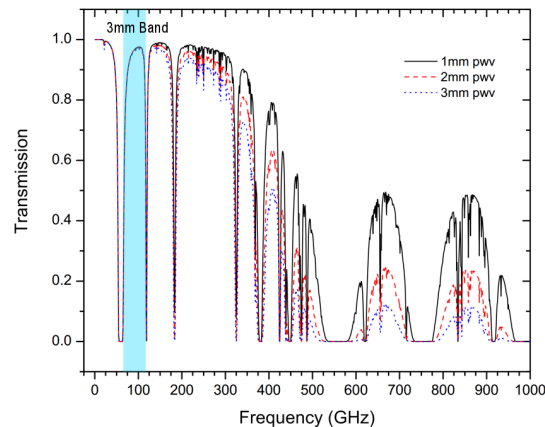
FIGURE 1.1: Simulated atmospheric transmission on Sierra Negra (LMT site) for different values of PWV. The 3mm Band is highlighted in blue. SOURCE: Ferrusca, 2006.

1.2 Millimeter Astronomy

As mentioned earlier, the radio window is a very broad window (from 1 THz (0.2 mm) to 10 Mhz (30m)) and as such, a single design of instrumentation is not able to fulfill all the needs. As a consequence, the instrumentation design is specialized in narrower ranges. Particularly, this thesis will focus in the millimeter range.

Some millimeter radio sources can be found at different scales from asteroids to circumstellar envelopes to the cosmic background radiation but the study of molecular clouds and molecular species are emphasized (Wall et al., 1999). Astrochemistry is a branch of astronomy that focuses in the synthesis of interstellar molecules and evolution of dense interstellar gas. A consequence of the latter is its role in the formation of stars and their later stages, hence the formation of planets and their early chemical composition and ultimately, the origin of life (Academies, 2015). Even though star formation can be considered to be part of astrochemistry, it has its own dedicated section due to its importance and the vast information found.

1.2.1 Astrochemistry and Molecular Astrophysics

Although the term *astrochemistry* is relatively new, it may have its origins in the detection of the first molecules in the InterStellar Medium (ISM). OH was first detected in 1963. It was followed by the discovery of ammonia and water. Finally, the detection of formaldehyde, H_2CO, gave hint about the chemical complexity of the ISM (Payne, 1989)

Astrochemistry mainly studies the formation, destruction and excitation of molecules in astronomical environments and their influence on the structure, dynamics and evolution of astronomical objects. (**Dalgamo2008**) Space provides a unique environment in which reactions between
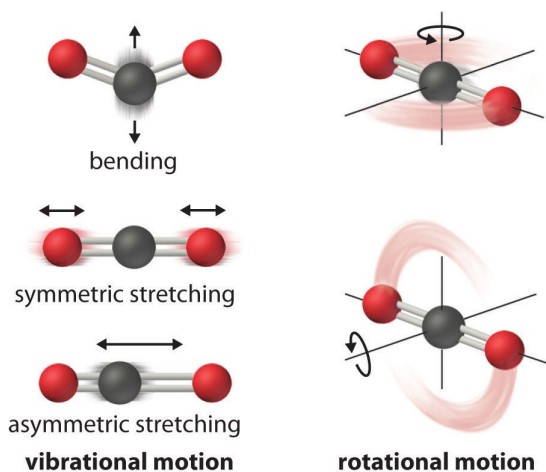
FIGURE 1.2: Graphical representation of a CO molecule's motion that produce the vibrational and rotational transitions. SOURCE: Chemistry: The Central Science (Brown et al.)

atoms is in a gas state and at very low densities unlike to Earth's environment. Also, these conditions permits the existence of molecules that are highly reactive on Earth (Estalella and Anglada, 1999). Consequently, astrochemistry search the answer to the following questions, a) How far does chemical complexity go? and b) How, when and where are these molecules produced and excited? To answer the first question, up to now, at least 200 different molecular species have been detected in the ISM. They span from simple diatomic molecules to molecules with up to 15 atoms such as $CH^{13}N$. Some characteristics observed are that most molecules are organic molecules and generally have a linear structure (Estalella and Anglada, 1999).

For the second question, the first mechanism proposed for molecular synthesis is gas-phase ion-molecule reactions which explains the abundance of most molecules in the ISM. Other mechanisms are neutral-neutral reactions, gas-phase reactions, grain-surface reactions and gas-grain interactions (Yamamoto, 2017).

Observational data has shown source to source variation which can be explain as a chemical evolution, a result that has justified the use of molecules as age tracers(Yamamoto, 2017). Also, some molecules can only be found in certain sources and at certain physical conditions which can provide insight of the physical conditions and processes from the regions they are in.

Molecules are a very complex system but by using the Born-Oppenheimer approximation, which consist in the separation of the nuclear and electronic motion, it can be broken down into simpler models. This approximation can be used due to the fact that the electron mass is much smaller than the nuclei mass and consequently the electrons adapt to the movement of the nuclei (Estalella and Anglada, 1999).

A molecule can present 3 different types of transitions: (Wilson, 2009)

- Electronic transitions are due to a change in the electronic cloud. This type of transition have energies of a few eV which makes them visible in the optical or UV window. This type of transition is also present in atoms.

- Vibrational transitions are caused by the oscillations of the relative position of the nuclei with respect the equilibrium position. This type of transition have energy on the order of 10×10^{-1} eV to 10×10^{-2} eV making it visible in the infrared window.

- Rotational transitions are produced by the rotation of the nuclei. This type of transitions have energies of the order of 10×10^{-3} eV. This type of transitions are observed in the millimeter and sub-millimeter window.

Most known molecules have been found through their rotational transitions. A search in Splatalogue showed that there are 37405 molecular lines in the range 85 GHz to 115 GHz (Remijan, 2010).

The CO molecule, the second most abundant after H_2, is chemically stable and has been found in the galactic plane and in other galaxies (Academies, 2015). The CO molecule can be used a tracer of H_2 and therefore can provide information about the molecular cloud structure, the disk around forming stars, and may even give us information about the conditions of planet formation. The 100-116 GHz band is used for CO redshift search in distant galaxies and also to observe the isotopic transitions ^{12}CO, ^{13}CO, and $C^{18}O$ in the Milky Way and nearby galaxies (Academies, 2015).

1.2.2   Star Formation: Galactic and Extragalactic Sources

In the present day, the studies of star formation are done at different scales from galactic sources (such as protostellar and protoplanetary systems, molecular clouds and star clusters) up to extragalactic sources (such as other galaxies, groups of galaxies and the first objects that re-ionized the Universe). As such, research on this topic is divided mainly into two separate groups: galactic and extragalactic. The galactic community focuses in the physical processes that determine the contraction and fragmentation of molecular clouds into clumps and cores within our galaxy, while the extragalactic community focuses on the collective effects of star formation in entire star formation regions.

Even though the physical processes of star formation are generally known at the different and particular scales observed, the connection between them is not yet well understood. This creates the need of an unified approach. (Kennicutt and Evans, 2012).

The InterStellar Medium (ISM) provide the seeds for star formation. The ISM is a very complex environment and is generally divided into 5 phases: 1) hot ionized medium, 2) warm ionized medium, 3) warm neutral medium, 4) cold neutral medium and 5) molecular clouds. The molecular clouds represent the coldest and densest part of ISM with values of $T_K \sim 10$ K and $n > 30$ cm^{-3}, respectively.

TABLE 1.1: Physical processes associated to star formation at different scales

Scale	Physical Process
Mpc	Accretion of gas onto galaxy's disk from intergalactic medium and satellite objects
kpc	Cooling of gas to form cool neutral phase
10 pc to 100 pc	Formation of molecular clouds
$\sim$1 pc	Fragmentation of molecular gas into clumps
$\sim$0.1 pc	Fragmentation of molecular gas into cores
$\sim R_\odot$	Contraction of the cores to form stars
$\sim$ AU	Subsequent contraction of the cores to form planets

Within molecular clouds, astrophysicist have observe filament structures with smaller and denser regions: clumps and cores. Clumps are larger regions than cores and are considered to be the birthplace of clusters, while cores are considered to be the birthplace of individual or binary stars. (Kennicutt and Evans, 2012).

The current approach to detect molecular clouds is by detecting radiation emitted by the different types of molecules that compose each of them.

The most abundant component of molecular gas is H_2. By observing this molecule, a deeper understanding of the dynamics and structure of molecular gas can be obtained. However, H_2 is difficult to observe since it only emits when exposed to high temperatures, which are rarely present within molecular clouds. Because of this difficulty, tracers are used to infer the properties of molecular gas. The CO molecule is the most common tracer of molecular gas due to its strong lines making it easier to observe.

To surpass the limits imposed by the fact that the ^{12}CO emission is optically thick, complementary observations of its isotopologues ^{13}CO and C^{18}O are commonly used. These combination has been used to estimate the optical depth which later gives the CO column density that can be correlated with the extinction to determine the conversion factor X(CO) (Kennicutt and Evans, 2012). The conversion factor X(CO) is used in extragalactic studies to estimate the column density of H_2 by $N(H_2) = X(CO)I(CO)$. Some values for the conversion factor found in the literature are 2.8×10^{20} cm^{-2} (K km s^{-1})$^{-1}$, 2.0×10^{20} cm^{-2} (K km s^{-1})$^{-1}$, or 2.3×10^{20} cm^{-2} (K km s^{-1})$^{-1}$.

Additionally, the luminosity of CO J=1→0 is a measure of cloud mass with linewidth reflecting the virial theorem in a crude sense(Kennicutt and Evans, 2012). When studying extragalactic sources, individual clouds can not be resolved so the luminosity of CO is used as a cloud counting technique assuming clouds have uniform properties. M = α_{CO}L (CO) where α_{CO} is the conversion factor of CO luminosity to the cloud mass. α_{CO} has been observed to not be the same at center of galaxies and within galactic objects. Moreover, it decreases by a factor 2-5 in nearby galaxy nuclei, a factor

5-6 in local UltraLuminous Infrared Galaxys (ULIRGs) and in high redshift galaxys(Kennicutt and Evans, 2012).

There have been different attempts to find a relation of α_{CO} to different physical properties of clouds in other galaxies, such as metallicity or surface density (Kennicutt and Evans, 2012). One example is given by Narayanan, Snell, and Bemis, 2012, where a grid of model galaxies is used to infer a smooth function of integrated intensity of CO: $\alpha_{CO} = \min \left[6.3, 10.7 \times I_{CO}^{-0.32} \right] Z'^{-0.65}$ where Z' is the metallicity divided by the solar value.

Additionally to CO, CS and HCN are also good tracers for dense gas. CS J=2→1 and HCN J=1→0 are molecular lines that lie in the 3mm band and which can be correlated to the virial mass of dense gas. This tracers' observations in conjunction with dust continuum emission have identified "dense clumps" which have a mass function similar to that of clusters (Kennicutt and Evans, 2012).

Mass functions of clusters and stars are presumably related to the mass function of their progenitors, clumps or cores. Studies of molecular clouds in nearby galaxies showed that the mass function appear steeper in the inter-arm regions than in the spiral arms, probably due to the aggregation of clouds into larger structures within arms and disaggregation as they leave the arms (Kennicutt and Evans, 2012).

Mass function of cores is steeper than that of clouds and similar to that of stars, suggesting that cores are the precursor of stars and that the mass function of cores set the mass function of stars. This does not happen in the case of clumps and clusters. One reason might be that clumps are not always gravitationally bound. For the latter studies, ground observations of dust and information of the velocity structure are needed to complete the picture (Kennicutt and Evans, 2012).

A common observed property across all of density regimes in galaxies show that star formation takes place in molecular clouds. Also, all star formation in molecular clouds are localized in clumps roughly defined by $\Sigma_{mol} > 125\,M_{\odot}\,pc^{-2}$ or n $> 10^4\,cm^{-3}$ (Kennicutt and Evans, 2012).

The limitation in the study of the global properties of multi-scale star formation processes, comes in part by the lack of the appropriate instruments to study in statistical significant samples the large scale structure of molecular clouds. Heterodyne array instruments, such as the one presented in this thesis, may help to overcome that limitation.

1.3   Radio Instrumentation

In radio astronomy, astronomers have two ways to measure the radiation, by measuring the continuum total power or by obtaining the Power Spectral Density (PSD). Each type of measurement uses a different type of radiometer being incoherent and coherent, respectively.

Incoherent Radiometers, also called continuum instrumentation, refer to those that do not pre-serve the phase of the signal. At millimeter wavelengths, the most common incoherent detector is the bolometer. A bolometer is a broadband detector that uses the change of temperature caused by the absorption of radiation. This temperature change does not depend on the polarization or on a specific frequency of the radiation. Therefore, bolometers are used for continuum observa-tions (Wilson, Rohlfs, and Hüttemeister, 2013).[1] Currently, continuum receivers are composed by an array of bolometers. The LMT has Astronomical Thermal Emission Camera (AzTEC) an 144-bolometer array sensitive at 1.1 mm band.[2] The LMT's next generation continuum instruments will be MUSCAT and ToLTEC, which is a ~6400 bolometers array conformed by 900 bolometers sensitive at 2.1 mm, 1800 at 1.4mm, and 3600 at 1.1 mm.[3]

Coherent Radiometers are the ones that preserve the phase of the incoming radiation and are sensitive to one polarization. Usually, the signal is mixed down from a high frequency to a lower frequency by heterodyne systems. A typical heterodyne system consist of a front-end, that shifts the signal to lower frequencies, and a back-end, that processes the lower frequency signal (Wilson, Rohlfs, and Hüttemeister, 2013). SEQUOIA is a heterodyne instrument developed by University of Massachusetts (UMass) and first commissioned to the Five College Radio Astronomy Observa-tory (FCRAO). At present, SEQUOIA will be commissioned to the LMT. In order to overcome the challenges of the scientific cases, a new back-end was developed named Wideband Array ROACH Enabled Spectrometer (WARES), which will be further explained in Chapter 2.

1.4 SEQUOIA

The SEQUOIA is an astronomical instrument developed by the UMass Millimeter Astronomy Labo-ratory in the mid 90's. It is a 16 pixels focal plane array for the 85 GHz to 115 GHz band. SEQUOIA was first installed in 1997 at the FCRAO 14-meter telescope (SEQUOIA, 2017). Later, it was joined by a second SEQUOIA with opposite polarization making, in total, a 32-pixel dual polarization in-strument.

In 2003-2004, SEQUOIA was used to create a high sensitivity ^{12}CO and ^{13}CO J=1$\rightarrow$0 molecular line maps covering the full extent of the parsec scale Haro 6-10 Herbig-Haro (HH) flow from which a molecular CO outflow was discovered (Stojimirović, Narayanan, and Snell, 2007). From November 2003 to May 2005, SEQUOIA completed a 98 sq. deg ^{12}CO and ^{13}CO map of the Taurus Molecular Cloud with a resolution of 48″ utilizing On-The-Fly (OTF) mapping. The goal of this map was to research the molecular gas distribution, interstellar gas dynamics and the star formation process. The ^{12}CO transition was used to track the lower column density while the ^{13}CO transition was used

---

[1]For more information on coherent radiometers, see Ch.5 of Wilson, Rohlfs, and Hüttemeister, 2013.
[2]http://www.lmtgtm.org/telescope/instrumentation/instruments/aztec/
[3]http://toltec.astro.umass.edu/about.php
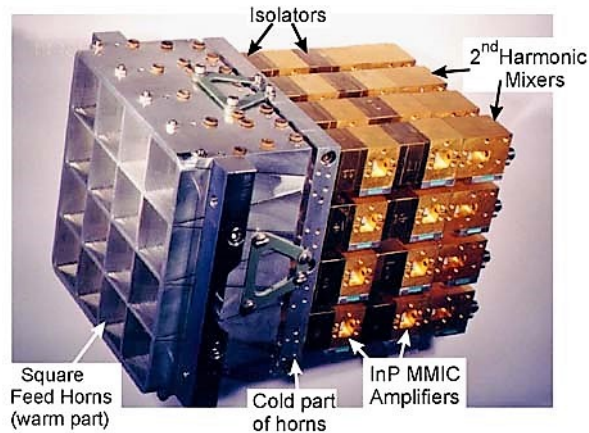
FIGURE 1.3: Picture of SEQUOIA main components. SOURCE: UMass Millimeter Laboratory's website.
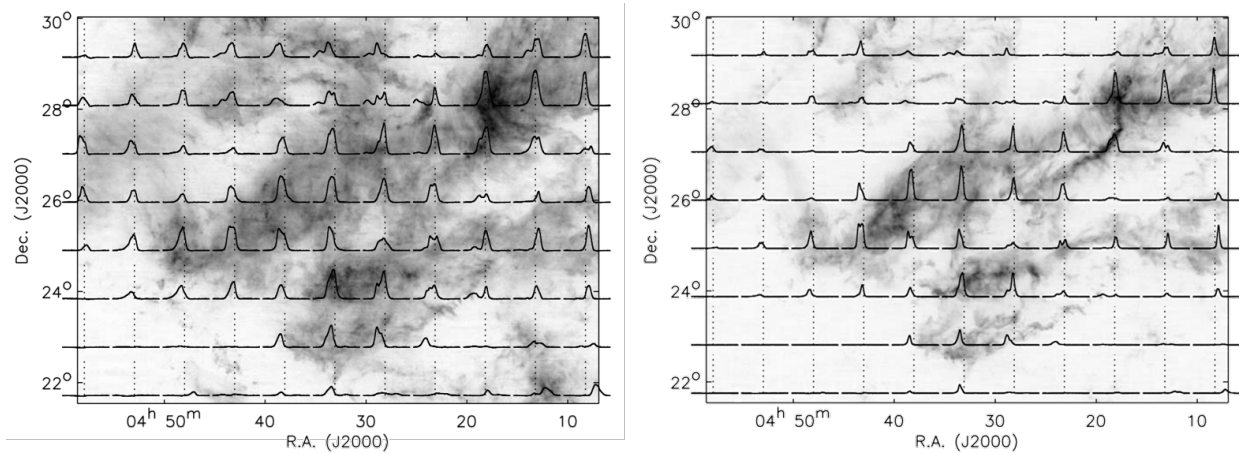
FIGURE 1.4: Mosaic of box-averaged spectra for ^{12}CO (left) and ^{13}CO overlaid on images of integrated intensity of Taurus Molecular Cloud. SOURCE: Fig. 20 of Narayanan et al., 2008.

to trace the underlying structure of the molecular cloud (Narayanan et al., 2008). The initial results of this survey were: (Goldsmith et al., 2008)

1. The molecular cloud showed very fine and varied structure such as blobs, holes, and filaments.
2. The total mass of the mapped region is $2.4 \times 10^4 \, M_\odot$ and half is contained in regions with column density $<2.1 \times 10^{21} \, cm^{-2}$
3. The average star formation rate calculated was $\simeq 8 \times 10^{-5} \, y^{-1}$.

Later in 2012, using the Taurus Molecular Cloud survey, 20 molecular outflows from Young Stellar Object (YSO) were identified from which 8 were new detections. From the dynamical time-scales calculated and the low detection of Spitzer Class I and flat spectrum sources, it was concluded that outflows appear in a short phase of YSOs and Taurus's YSO are older (Narayanan, Snell, and

FIGURE 1.5: Photograph of LMT. Comparison of the LMT's size to a person's size.

Bemis, 2012). This survey also show that outflows are not energetic enough to produce the cloud turbulence seen.

1.5 Large Millimeter Telescope (LMT)

The LMT is a 50m radio telescope at an altitude of 4600 m in Sierra Negra, Mexico. This telescope is the world's largest single dish telescope for millimeter observations in the 0.85 mm to 4 mm range. It is a bi-national project between Mexico and the United States lead by Instituto Nacional de Astrofisica, Optica y Electrónica (INAOE) and UMass-Amherst (INAOE, 2016).

The LMT site is an extinct volcano within the National Park of Pico de Orizaba near the border of Puebla and Veracruz. Also, at a latitude of 19°, it provides a good coverage of the southern sky that permits a culmination of the galactic center at an elevation of 45° (**Schloerb2008**). The altitude of 4600 m makes the site to have very low opacities from <0.06 up to 0.28 on the driest months (Zeballos et al., 2016), ideal for millimeter and sub-millimeter observations.

The first light instruments of the LMT are the Redshift Search Receiver (RSR), SEQUOIA, and AzTEC. Both the RSR and SEQUOIA are heterodyne instruments, while AzTEC is a continuum instrument.

SEQUOIA with the LMT will provide complementary characterization of the molecular and dense gas on large scales than can be efficiently surveyed with arrays such as ALMA. SEQUOIA with the LMT will aid in search of answers in star formation and in the search of organic molecules in the

universe. SEQUOIA can contribute to the understanding of star formation by doing CO J=1→0, ^{13}CO, CS J=2←1 and HCN J=1←0 maps of molecular clouds within the Milky Way. These maps in combination with other surveys at different wavelengths will improve the overall image of the dynamic structure of the gas which can later serve as a template for other galaxies. Additionally, it can track different molecules that will serve as tracers to understand the morphology and dynamic of protoplanetary systems. Moreover, in the study of planets it can detect organic molecules which will mean the presence of life or elements of life. With the study of comets, we can study the elements that composed the interplanetary medium and give more hints of organic molecules.

1.6 This Thesis

This thesis details the process followed during the modification and integration design for Wideband Array ROACH Enabled Spectrometer (WARES), a wideband, FPGA-based spectrometer which will become SEQUOIA's new back-end. When fully equipped, WARES will be able to simultaneously process 32 input signals and record the resulting data into a hard drive for analysis. This is achieved by creating a system with FPGA boards and ADC cards from the CASPER group which will be able to handle all inputs signals from SEQUOIA.

The objectives of this thesis are:

1. Develop a Polyphase Filter Bank spectrometer code using the CASPER tools for each operation mode.

2. Characterize the spectrometer by inputting a known signal. This characterization includes the ADC parameters following the IEEE standard, linear range and stability test.

3. Calculate the receiver temperature by connecting the spectrometer to SEQUOIA and perform the stability test.

This thesis will describe the hardware and software tools needed for the development of WARES on Chapter 2. Later, it will explain the FPGA designs that operate SEQUOIA with spectrometer in Chapter 3. Also, it includes the procedure of characterization tests made to a WARES module and its integration with SEQUOIA in Chapter 4 and Chapter 5, respectively. Finally, in Chapter 6, it will describe the pending tasks to integrate SEQUOIA with the LMT.

Chapter 2

WARES Hardware and Software

SEQUOIA needed a new back-end with upgrades in spectral bandwidth, resolution and data rates which are necessary for an optimal integration with LMT. Wideband Array ROACH Enabled Spectrometer (WARES) is the name given to the back-end of SEQUOIA and it is a Field Programmable Gate Array (FPGA) based spectrometer. It will expand the previous back-end's baseband of 50 MHz to 200 MHz and add two additional operation modes with basebands of 800 MHz and 400 MHz. It will be able to handle the 32 signals coming from SEQUOIA and the data rate will be enough to use OTF mapping.

WARES was developed with the hardware and software tools provided by the Collaboration for Astronomy Signal Processing and Electronic Research (CASPER), a radio astronomy group from the University of California, Berkeley and their main objective is to provide hardware and software tools to facilitate the development of modular and reconfigurable instrumentation for radio astronomy by promoting the design reuse of open hardware and software. Since the creation of CASPER, it has been implemented in about 45 projects worldwide, such as the digital back-ends of the Five-hundred meter Spherical Aperture Telescope (FAST), the SMA Wideband Astronomical ROACH2 Machine (SWARM) correlator and phase array for the Sub Millimeter Array (SMA) and the VErsatile GBT Astronomical Spectrometer (VEGAS) spectrometer on the Green Bank Telescope (GBT) (Hickish et al., 2016). The main advantage of CASPER is the modularity of its hardware as well as the open source libraries and scripts provided for faster and easier development of radio astronomical instrumentation. Additionally, it has an active community who provides support and helps create a knowledge database from the member's experiences and projects.

WARES will consist of a main chassis with 8 modules. Each module is mainly comprised of a CASPER's ROACH 2 Board and two ADC1x5000-8 ADC cards. These among other hardware in use are described in Section 2.1. Furthermore, the description of CASPER software toolflow used for WARES development as the description of the WARES python class created to integrate with the LMT controls can be found in Section 2.2.
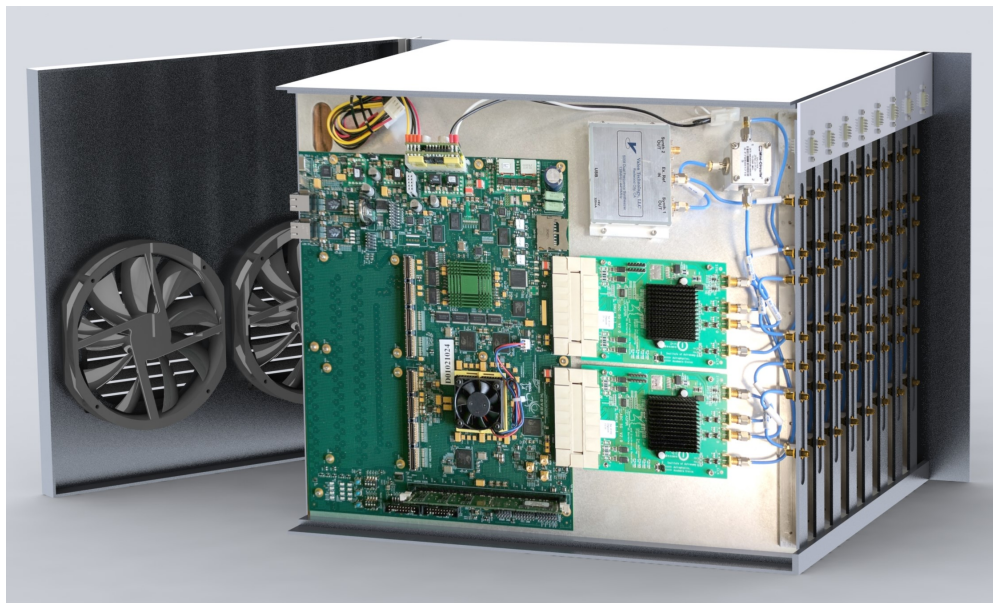
2.1   Hardware

FIGURE 2.1: CAD model of WARES featuring a module with its components, the power distribution plate and ventilation system. Note that it is cutout view of the chassis allowing to visualize a module's components.

WARES is composed of a main chassis with enough slots for 8 modules. Figure 2.1 features the chassis subsystems such as the ventilation system and the power distribution plate, as well as a cutout view to the components of a WARES module. The chassis' and the module's main features and components are described in the following sections.

2.1.1   Chassis

CASPER usually provides an 1.3U enclosure for mounting in a 19" rack cabinet which can hold one ROACH 2 Board.[1] This enclosure provides RFI protection and a ventilation system. However, the previous characteristics were not ideal for WARES due to two considerations. One is the space limitation at the LMT backend room. Eight CASPER's enclosures would have required 712 mm plus the space needed for the rest of the SEQUOIA's backend (IF processors, synthesizers, computers, etc.) and future instrumentation such as OMAR. Because of these reasons, space is a valuable resource which needs to be optimized. The second consideration is the ventilation system. From the CASPER mailing list, it was known that the provided ventilation system eventually fails when working at extreme conditions similar to those of the LMT site. As a result, the UMass team decided to design a new enclosure to diminishboth problems.

---

[1]https://casper.berkeley.edu/wiki/ROACH_2_Enclosure

TABLE 2.1: List of components for a WARES module

Item	Description	Quantity
1	ROACH 2 Board	1
2	ADC Card Model:ADC1x5000-8	2
3	Valon 5008 Dual Frequency Synthesizer	1
4	Power Supply Model: picoPSU-120	1
5	Power Splitter for Clock Model:ZFSC-2-11	1
6	SMA Cable Model:086-2SM	1
7	SMA Cable Model:086-3SM	2
8	SMA Cable Model:086-4SM	5
9	SMA Cable Model:086-10SM	1
10	SMA Cable Model:086-10MRSM	1
11	Bulkhead Connectors Model:SF-SF50	7
12	Connector DSUB9	1
13	Module Base Plate	1

In Figure 2.1, a CAD model of the new design is shown. It includes a chassis which will hold up to 8 modules, with ROACH 2 boards, in a space where, otherwise, there would only have been 4. In addition, it provides a more robust ventilation system composed of two powerful fans in the chassis's door which will move the airflow from front to back. A power distribution plate is also provided as a solution to distribute the different voltages needed to power each module. Furthermore, this design provides an easier way to give maintenance to the boards.

2.1.2 Module

As mentioned previously, WARES will include 8 modules. Each module is composed mainly of a ROACH 2 Board, two ADC1x5000-8 ADC cards, a clock synthesizer with a 2-way splitter and a DC-DC power supply. Additional hardware in a WARES module is listed on Table 2.1.

Reconfigurable Open Architecture Computing Hardware (ROACH) 2 Board

The ROACH 2 Board is a processing board based in a Xilinx® Virtex 6 Series FPGA. A Field Programmable Gate Array (FPGA) is a reconfigurable integrated circuits that consists of an array of programmable logic blocks and reconfigurable interconnect (Price, 2016). In addition, it includes Block RAM (BRAM) which are large *blocks* of memory distributed throughout the FPGA. The Virtex 6 FPGA provides 476K logic cells and 38Mb of BRAM. The ROACH 2 Board has an increased processing and I/O capabilities than its predecessor (Hickish et al., 2016). It also includes a PowerPC 440EPx stand-alone processor providing an intermediary between the user computer and the
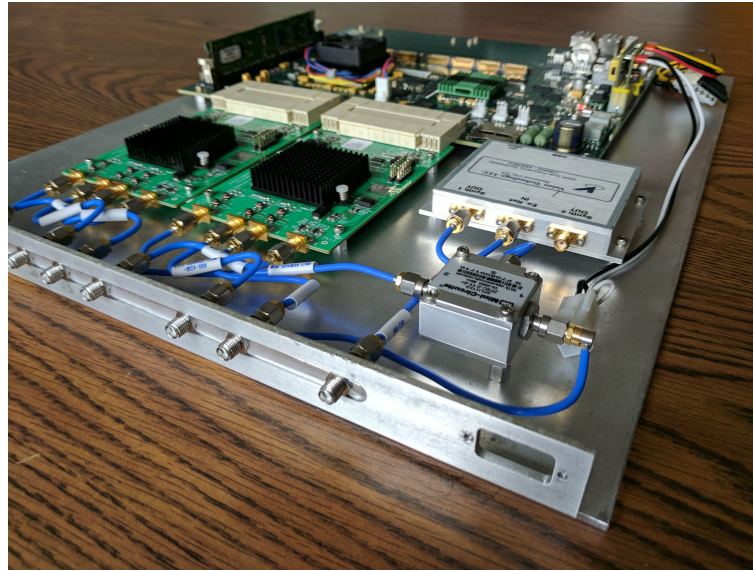
FIGURE 2.2: Photograph of a WARES Module.

FPGA. As part of its modularity, it includes two ZDOK connectors which can be used to connect different ADC or DAC cards, according to the project needs. Additionally, it allows the connection of *Mezzanine* boards to increase the Ethernet connections and rate to 8x10 GBe.[2]

Analog to Digital Converter (ADC) Card

The selection of the ADC card was mainly determined by the acquisition rate needed which was determined by the Nyquist theorem. The Nyquist theorem says that the sampling frequency needs to be at least 2 times the maximum expected frequency of the signal to be fully reconstructed. The output of the Baseband IF processors has a band of either 800 MHz, 400 MHz or 200 MHz. Therefore, the selected ADC card must have at least an acquisition rate of 1600 MHz (2 times 800 MHz). With this in mind, the ADC card chosen was the ADC1x5000-8. [3] This card provides a single 8-bit 5 GSPS input or a dual 2.5 GSPS input. This ADC card is based on the EV8AQ160[4] chip by Teledyne e2v®[5]. This chip is composed of four 8-bit 1.25 GSPS ADC cores. In dual-input mode operation, two of these cores are grouped together to achieve a sampling rate of 2.5 GSPS by interleaving each core at half the frequency. In other words, two cores receive the same input signal but the clock is divided by two and inverted for one of the cores. Figure 2.3 shows the block diagram of this mode. The dual input operation mode is enough to meet our needs. In addition, this mode will allow us to use 2 inputs per ADC hence 4 inputs per WARES module.

---

[2]For a list of compatible boards visit https://casper.berkeley.edu/wiki/Hardware
[3]http://casper.berkeley.edu/wiki/ADC1x5000-8
[4]http://casper.berkeley.edu/wiki/images/1/19/Ev8aq160.pdf
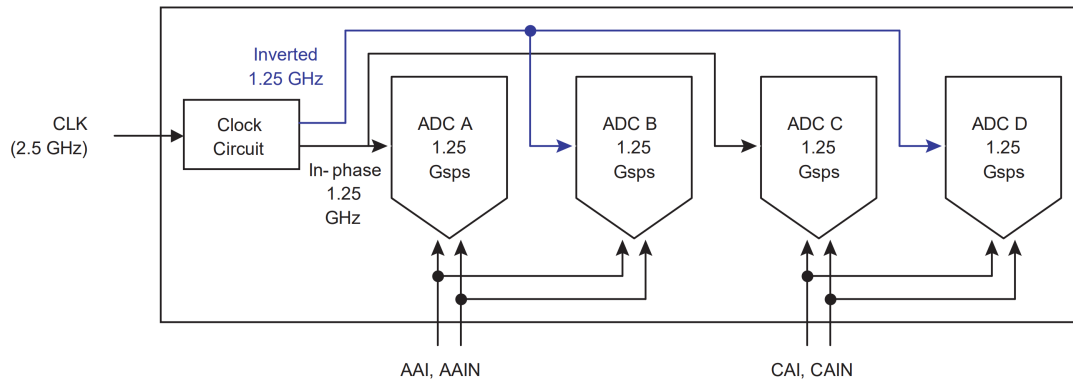[5]http://www.e2v-us.com/

FIGURE 2.3: Block diagram of dual input operation mode extracted from the datasheet of ADC chip model EV8AQ160 by Teledyne e2v. Note that Core A and B are grouped to form one output at a sampling rate of 2.5 GSPS while Core C and D correspond to the second output.

This ADC has been already proven to be useful for astronomy data since it has already been used in SMA and VEGAS instruments (Patel et al., 2014; Jiang et al., 2014). Based on these papers, the alignment of the cores proved to be an important step for the correct acquisition of the signal. This chip has the advantage that it provides control over three different parameters used in the alignment process: offset, gain and phase. These parameters are later referred as OGP parameters and their alignment process will be explained in detail Section 4.1.1.

Clock Synthesizer

Each ROACH 2 Board will use a synthesizer to set the clock for both ADC cards. Valon Technology, LLC offers a variety of low-cost and compact synthesizers for high quality clock, or local oscillator frequency generation applications from which it was decided to use the 5008 Dual Frequency Synthesizer.[6] This synthesizer has a programmable output frequency from 137.5 to 4400 MHz ideal for WARES since it will need a 1600 MHz and 800 MHz clocks. Also, this synthesizer has the ability of retaining the frequency setting after a power down and it includes a USB serial interface for communication from the main control computer. Finally, its dimensions are 67.7 mm × 91.7 mm × 13.2 mm making it small enough to fit in a WARES module. The output is controlled via a python wrapper included in the WARES class. It is powered with 6V provided from the power distribution plate from the chassis.
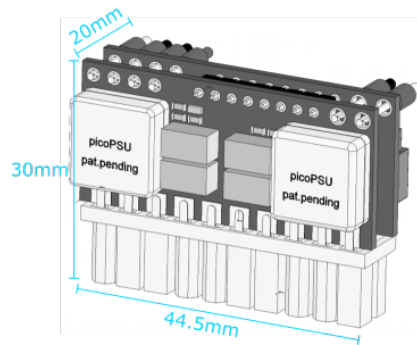
FIGURE 2.4: Dimension drawing of power supply model picoPSU-120 by Mini-Box.
Drawing extracted from user manual modified to include dimensions.

DC-DC Power Supply

A ROACH 2 Board can be powered by a normal PC Power Supply but its size and weight made it
not a portable option. Instead, each ROACH 2 board will use a picoPSU-120[7] by MiniBox[8]. This
is a DC-DC ATX power supply. This means that it provides 3.3V, 5V and 12V outputs according to
the ATX specification. Instead of powering it with 120 VAC as in the normal version, it will use an
external 12V DC power supply provided from the power distribution plate on the chassis.

2.2   Software

The CASPER's software tools needed can be classified into two categories: MSSGE Toolflow and
Communication and Control Tools. The first are the main tools use for the development of the
FPGA designs. The second are the tools needed for communication and control of a WARES Mod-
ule. Figure 2.5 shows the interaction between the software tools used.

2.2.1   MSSGE Toolflow

Matlab, Simulink, System Generator and EDK (MSSGE)[9] are the tools used for creating an FPGA
model design into an executable design. Simulink® is a block diagram environment which allows
to design and simulate systems.[10] Since it is integrated with Matlab® [11], it also allows to incor-
porate Matlab® algorithms as models into the design. The System Generator[12] is a Xilinx® tool

---

[6]http://valontechnology.com/5008/5008_DS.pdf

[7]http://www.mini-box.com/s.nl/it.A/id.417/.f

[8]http://www.mini-box.com/site/index.html

[9]http://casper.berkeley.edu/wiki/MSSGE_Toolflow

[10]https://www.mathworks.com/products/simulink.html

[11]http://www.mathworks.com/products/matlab.html

[12]https://www.xilinx.com/products/design-tools/vivado/integration/sysgen.html
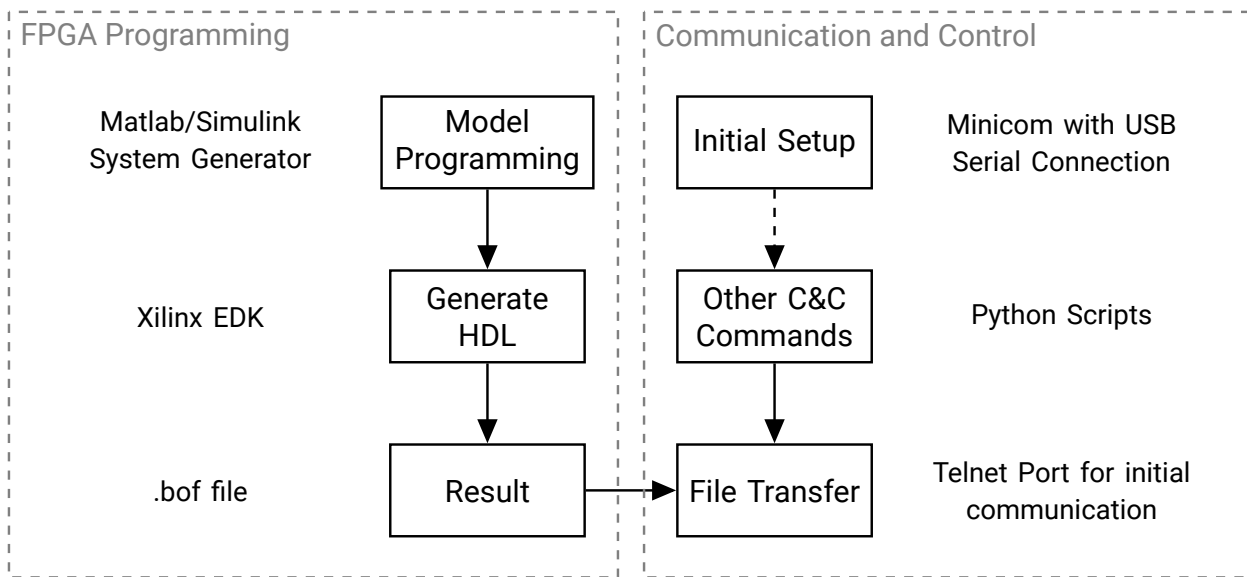
FIGURE 2.5: Diagram with the relationship between software tools

TABLE 2.2: List of version of the MSSGE tools used to develop WARES's FPGA designs.

Tool	Version
Matlab / Simulink	2012b
System Generator	14.5
EDK	14.5
Ubuntu OS	14.04
CASPER library (sma_mlib_devel)	a288ff3

for the creation of Digital Signal Processing (DSP) systems in Simulink®. It is a set of blocks organized into different function-specific libraries as well as an interpreter for passing from the Simulink® block diagram code into a Hardware Description Language (HDL) code. The Xilinx® Embedded Development Kit (EDK)[13] is a set of tools and Intelectual Property (IP) that enables to design a complete embedded processor system for implementation in a Xilinx® FPGA device (Xilinx, 2013). In other words, it provides the tools necessary to transform the HDL code into a bitstream file that can be implemented in the FPGA.

In Table 2.2, you can see the versions of the MSSSGE tools used for the design of WARES's FPGA codes.

In addition to the tools described before, CASPER also provides its own set of blocks divided into

---
[13]https://www.xilinx.com/products/design-tools/platform.html

two libraries: DSP library and XPS library.[14] The CASPER XPS is also called the "yellow block" library. This library includes blocks that are interfaces with hardware such as ADCs blocks, Ethernet blocks, or memory blocks. The CASPER DSP is the one that includes blocks, mostly identified by a green color, for the signal processing such as filters and FFT blocks. Both libraries are open source and it also includes block created originally from other CASPER based projects that turn out to be a useful function.

2.2.2   Communication and Control Tools

All communication to a ROACH 2 board is done by Ethernet so previously we had to assign an specific IP address to the board. For this, we first used a serial connection through the USB connector on the ROACH 2 board. The connection is made by using Minicom,[15] a terminal based serial port communication program.

After the IP address is set, the connection to the board is established by using TELNET through port 7147. This can be done from any terminal in any computer inside the local network. Port 7148 is exclusively used for bitstream file transfers.

In addition, CASPER recommends using python and the Corr libraries for communication and control. The Corr libraries were made by the SKA team for this purpose.

Finally, many python wrappers were created to interact with other instruments that are part of the SEQUOIA system such as the Local Oscillators (LOs), the Valon synthesizer, the IF processors and chopper.

2.2.3   WARES Python class

When SEQUOIA and WARES are installed on the LMT, it will need an easy way to be called from the control room. For this purpose, a Python class Wares was created. It can be acquired from GitHub.[16] This class includes the python libraries needed to communicate to the ROACH 2 board such as the corr library as well as the libraries and python wrappers to communicate to the IF processors, LO synthesizer and Valon synthesizer.

To initiate a instance for a WARES module you need to initiate the class with the specific IP Address of that module and also include the desired operation mode. When initiating your spectrometer instance several steps will happen. First, it will load the correct FPGA design depending of the operation mode. Then, it will configure the settings needed to initialize the FPGA designs. Finally, it will load default OGP and INL values for the ADC calibration.

---

[14]https://github.com/casper-astro/mlib_devel
[15]http://help.ubuntu.com/community/Minicom
[16]https://github.com/umass-wares/wares

CODE 2.1: WARES class initialization example

```python
from wares.spectrometer import Spectrometer
spec = Spectrometer('xxx.xx.xx.xx', mode=800, scale=256,
    default_ogp_file='/path/to/ogp_file.npz',
    default_inl_file='/path/to/inl_file.npz', gain=0xfffff)
```

Once initialized, the class can be used by appending the class alias to the function to be called. Some functions are:

snap(input)   Takes the ADC's raw data from the specified *input*.

integrate(input) Takes the spectra of the signal on *input*.

roach   Calls the Corr Class within the WARES class. This class allows some basic functions of the roach such as programming it.

This class was used, debugged and improved while doing the characterization tests described on Chapter 4 and Chapter 5.

Chapter 3

WARES FPGA Designs

The FPGA Designs are coded using the MSSGE tools, as explained previously. WARES will have 3 modes of operation which corresponds to the filters in the Baseband IF processors: 800 MHz mode, 400 MHz mode and 200 MHz mode. For each mode, there is a different FPGA design which will be loaded to the FPGA as needed. The main difference between this modes is the FFT size. Table 3.1 shows the FFT size for each operation mode and the equivalent spectra resolution. The first design created was the 800 MHz mode, and thus served as the base code for the rest of the operation modes.

Figure 3.1 shows a snippet of the 800 MHz FPGA design and is divided into 5 modules for ease of explanation. Each module is composed of function blocks and the interaction between blocks is given by the connection lines. Generally, the data flow will be from left to right and events will happen in parallel. The general modules are numbered 1 to 4 and are common to all three FPGA designs. Furthermore, this figure only shows the signal path of one spectrometer input since all inputs are equal. The signal path will be explained in Section 3.2.

3.1 General

Modules 1 to 4 are the same for all three operation modes.

TABLE 3.1: Comparison of operation modes of WARES

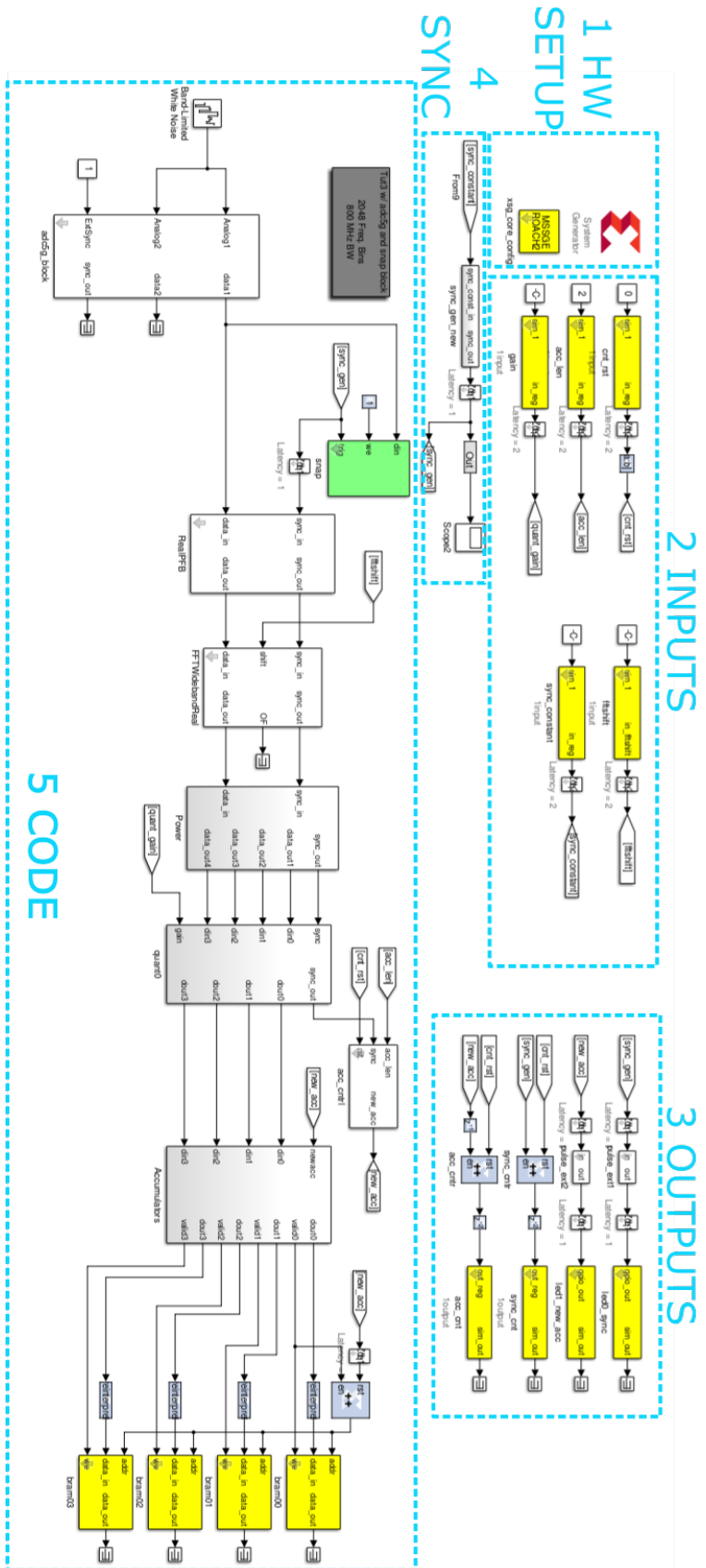| Operation Mode MHz	FFT size	Spectral Resolution $\mathrm{km\,s^{-1}}$
800	2048	1.3
400	4096	0.3
200	8192	0.07

FIGURE 3.1: This is the design for the 800 Mhz Mode. Note that it only shows one input of the 4 inputs available in a WARES module.

The first module is the HW Setup and is essential for every design based on CASPER. It is composed by the System Generator block and the XSG_core_config block. The System Generator is in charge of specifying the hardware settings of the FPGA in use and is configured by the XSG_core_config block. The latter block is provided by the CASPER library and has specific hardware parameters based on the processor board being used, in this case, the ROACH 2 board. Additionally, it allows selecting the source of the FPGA clock which in this case is selected to be the ADC cards in the first slot.

The second and third modules are to define the inputs and outputs, respectively. These modules exist mainly to keep the code clean and organized. Every input and output used by the code is declared in this area. The inputs and outputs can either General Purpose Input/Output (GPIO) or software registers. A GPIO is a physical input or output connected to the FPGA. A typical output of this type is a Light-Emitted Diode (LED) used as an indicator. A software register is specific section of memory in which a value can be stored. A reference tag is common to all inputs and outputs and has the purpose of sending the input or receiving the output values to anywhere in the code.

The fourth section is the Sync pulse. As data is constantly flowing through the blocks, a pulse is needed to framed the data to produce a valid block output. The sync pulse is used for this. It is defined as a reset signal that is offset one clock before the beginning of a every data frame (Henry Chen and Parsons, 2008). Several blocks from the CASPER library have an input and output for the sync pulse which allows them to add latency to the pulse as needed to keep it synchronized. The sync pulse period is calculated by Equation (3.1).

$$syncPeriod = G \times N_{accum} \times PFB_{taps} \times LCM(r\_o) \times \frac{FFT_{size}}{FFT_{inputs}} \qquad (3.1)$$

where: G = the gain specified by the operator,
       N_{accum} = the desired number of accumulations set by the operator,
       PFB_{taps} = the number of taps in the PFB block,[1]
       $LCM(r\_o)$ = the Least Common Multiple of the reorder orders inside the FFT block,[1] and
       FFT_{inputs} = the number of simultaneous inputs of the FFT block.[1]

The sync pulse is specially important for the correct operation of both the PFB and FFT blocks.

3.2   Signal Path

The fifth section is the Signal Path. As mentioned earlier, Figure 3.1 only shows the signal path for one input. Nevertheless, all other inputs are exactly the same.

---

[1] These parameters are further explained in Appendix **??**

The signal path starts with the ADC Block. This block is in charge of reading the output of the ADC cards. The ADC cards send 8 streams of 8-bits which represent consecutive values of our sampled signal. This 8-bit values are changed into 2-complement so negative values can be represented. This data is packed into a bus which goes into the next blocks. The input of the ADC block is a white noise generator and is used for simulation purposes only. The output of this block are two data streams, one for each input.

After the ADC block, the data stream is sent to two blocks, the Snap block and the PFB Block. The Snap block provides a direct way to read the values of the signal right after it has been digitized. It takes the data and saves it into a BRAM. A BRAM is a type of random access memory that is embedded throughout an FPGA for data storage and is mainly used to store a large quantity of data (NI, 2016). The data stored is used for the ADC's characterization explained in Chapter 4.

The PFB block with the FFT block implements a Polyphase Filter Bank (PFB). A PFB is simply an efficient computational structure used to form a bank of filters. The PFB front-end enhances the filter response of the FFT, making it better by using time samples and filter coefficients (Price, 2016). The advantages of using a PFB is to reduce spectral leakage and scalloping losses. [2] The filter coefficients represent a type of window. Windows are used to sharpen the filter response of the DFT. This is achieved by approximating a sincfunction in the time domain. Each windows has coefficients that approach this sinc function. The windows selected for this is the Hamming window.

Figure 3.2 shows how the PFB front-end works. First, the incoming signal with N samples is divided into M taps of P points where $M \times P = N$. The window coefficients are also divided into M taps with P points each. Then, it multiplies the signal and the window point by point. Later, all taps are summed together that results in a filtered signal of P points. This filtered signal is the output of the PFB block and is later sent to the FFT block. For the next output, the taps sections are moved into the following tap. In the figure, the signal's tap sections are moved from left to right. Hence, in tap M=3, new P data points appear. This process continues until all samples in the data frame hasve passed through.

The output of the FFT block is in complex numbers. So the PSD is calculated by taking the square root of the sum of the square of the imaginary part and real part. This is done in the Power Block. Then, the PSD is quantized by the Quant block. This means that each value is mapped into a lower bit value. In this application, the 32-bit value is quantized into 6.5 bits value.

After being quantized, the PSD is accumulated in the Accumulation block. The accumulation time is defined by the acc_len. The acc_len is a software input and is set during the configuration of the operation mode when using the WARES class. An advantage of the quantization process is to prevent the saturation of the accumulated spectra.

---

[2] https://casper.berkeley.edu/wiki/GPU_Tutorial:_PFB

Input data stream

Filter coefficients

4P   3P   2P   P   0

4P   3P   2P   P   0

m=3   m=2   m=1   m=0

×   ×   ×   ×

=   =   =   =

Σ

P   M=3   0

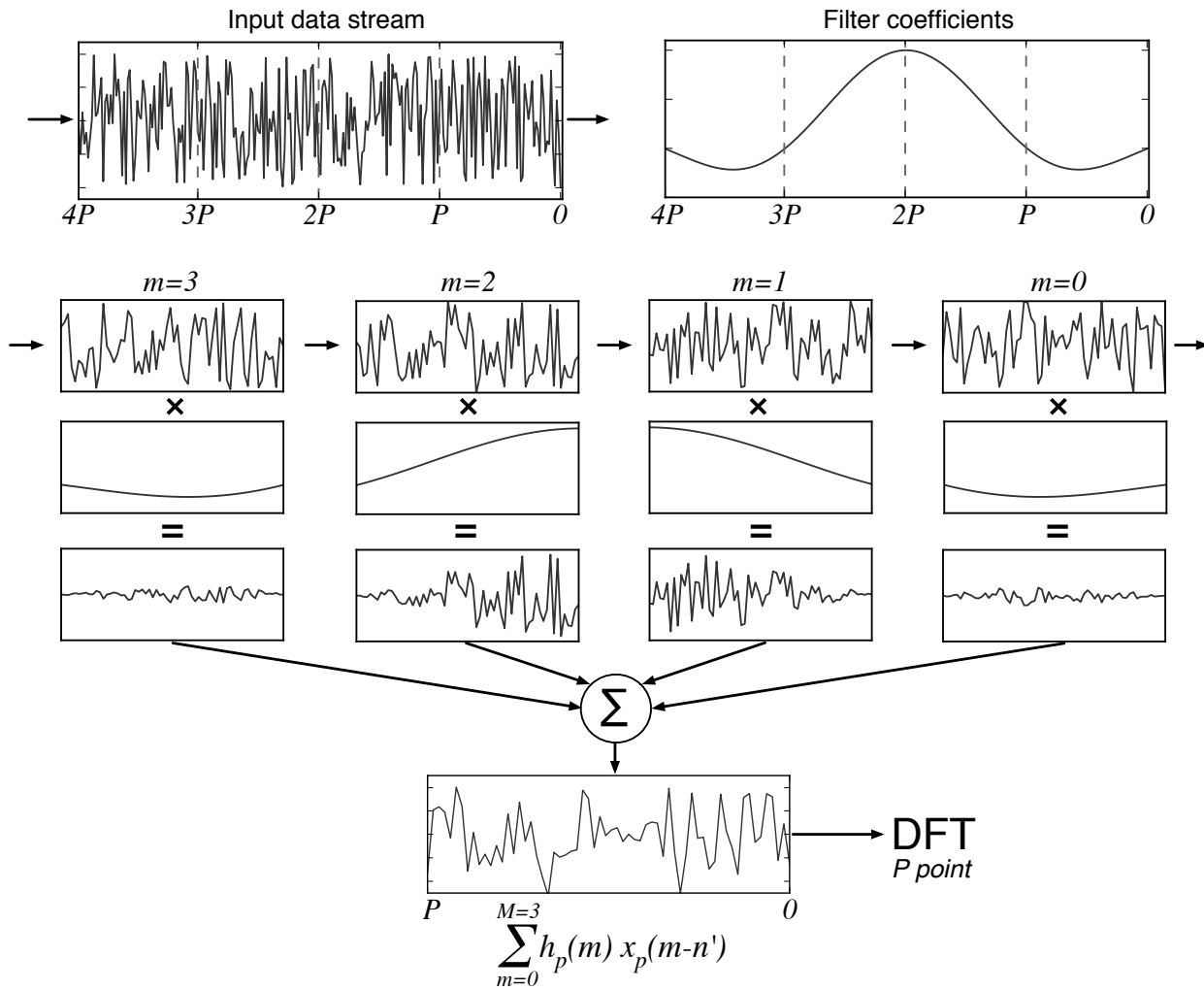$$\sum_{m=0}^{M=3} h_p(m)\, x_p(m\text{-}n')$$

DFT
P point

FIGURE 3.2: Graphical representation of a PFB filter obtained from Price, 2016.

Finally, the accumulated spectra is saved into BRAMs, from where it can be read from the control computer.

3.3   Operation Modes Differences

The main difference between each mode is the FFT size. The FFT size sets the resolution at each operation mode. (see Table 3.1). The FFT size also affects the PFB block and the FFT block, and consequently the sync period and the accumulation length.

The 800 MHz mode has a sampling rate of 1600 MHz while the 400 MHz and the 200 MHz have a sampling rate of 800 MHz. The sampling rate of 800 MHz is the lower limit for our ADC clock since the FPGA clock is 1/8 of the ADC clock whose minimum clock is 100 MHz. So to achieve a sampling rate of 400 MHz, the 200 MHz mode uses every other data point from the ADC. By interleaving the output of the ADC block, the streams of data that get into the following blocks are reduced. This new number of inputs and outputs is a parameter that needs to be changed throughout the block in the code.

Finally, since the 200 MHz has 8192 points per FFT, it becomes more computationally expensive. For this reason, the number of taps was diminished to 2 taps instead of 4 taps used in the other modes.

3.4   Black Boxing

In the previous section, we have talked about the code which is created by using the following tools Matlab® Simulink® and System Generator. For the compilation process, the EDK tool by Xilinx® is also used.

To start the compilation of a design, in the Matlab® terminal we run the command run casper_xps. This will open a dialogue box where we need to specify the .slx file we are compiling.

The duration of this process varies proportionally to the complexity of the design. A single channel design is compiled in around 15 min or less, while a full four input design might require as much as 10 hours of compilation time.

Timing errors are the most common type of problem presented in this stage of the designing process. The simple fix was to include latency block between the affected blocks. The difficult fix was to use the tool Plan Ahead to manually analyze and move the affected blocks.

The design compilation was time consuming and, in the end, there was no guarantee that it would work. To avoid these long periods of death time, a methodology was developed in which a simple

TABLE 3.2: Comparison of compilation times before and after black boxing the 4 inputs designs. The times are average of the compilations needed.

Operation Mode / MHz	Before /h	After /h
800	3	1
400	6	0.93
200	>10	0.8

single input design for each mode was compiled, at first. Once its problems were resolved, a 2-input design was compiled, followed by the compilation of the 4-input design. However, this meant that, if a change was necessary on the last step, the compilation methodology needed to start all over. This approach didn't attack the real problem of minimizing the death time.

It is known that most of the time in the compilation process is consumed by compiling very heavy blocks such as PFB and FFT blocks. This is mainly because each block is being generated and synthesized separately even though it is a repeat of a block already compiled (MacMahon, 2010). As a result, the heavy blocks are compiled up to 4 times each which consequently means long compiling time even when the changes are nothing to do with these blocks.

Xilinx® provides a solution called Black Box. This method allows to create blocks of different parts of the code. Its main advantage is that these blocks are compiled independently of the main code making the main code compilation time shorter. Also, every black box of the same function will be exactly the same since its loading the same netlist. It is recommended to use this method when the design has repetitive functions and also in very heavy blocks like PFB and FFT. For our designs, they were used for the PFB block and FFT block. For every different black box used in a design it will have the following associated files at the same level as the main design file.

- function_core.mdl (or .slx file),
- a folder with the same name,
- a function_core_config.m file,
- and function_core.vhd file

After implementing the black box method, the compilation time decreased dramatically. In Table 3.2, a comparison between compilation times before and after black boxing the design is shown. Additionally to minimizing compilation time, this method also proved useful to optimize the designs so that the designs stop showing timing errors.

Chapter 4

WARES Characterization

This chapter will describe the tests applied to a WARES module. These tests represent future work that has to be done to each individual WARES module once they exist before a full test with SEQUOIA. This test are needed for the initial setup.

As mentioned previously, a WARES module primarily consists of a ROACH 2 Board, a Valon synthesizer, and two ADC cards. In addition, for the WARES testing, a 1 GHz noise box, a synthesizer, 4-way splitter, a 2-way splitter and a mixer were used.

The WARES tests are divided into 3 sections. The ADC characterization ensures the correct acquisition of the signal as explained in Section 4.1. The linearity Test, or dynamic range test, is used to determine signal's power level range that can be input to the WARES module for it to be detectable and is explained in Section 4.2. Lastly, the stability test, explained in Section 4.3, is used to determine the maximum integration time that the signal can be integrated by before losing the signal's integrity.

4.1 ADC Characterization

The ADC characterization was based on the paper of Patel et al., 2014. It states that for a complete ADC characterization, it first needs a core calibration or alignment. This process will be discussed in Section 4.1.1. After the calibration is completed, the characterization test is started with the measurement of the Spurious-Free Dynamic Range (SFDR), SIgnal to Noise And Distortion ratio (SINAD) and Effective Number Of Bits (ENOB), whose process is explained in Section 4.1.2.

4.1.1 Offset, Gain and Phase (OGP) Calibration

The ADC calibration main objective is to ensure the signal is being acquired correctly. As mentioned in Section 2.1.2, the ADC card is being used in its dual mode where one input is fed into
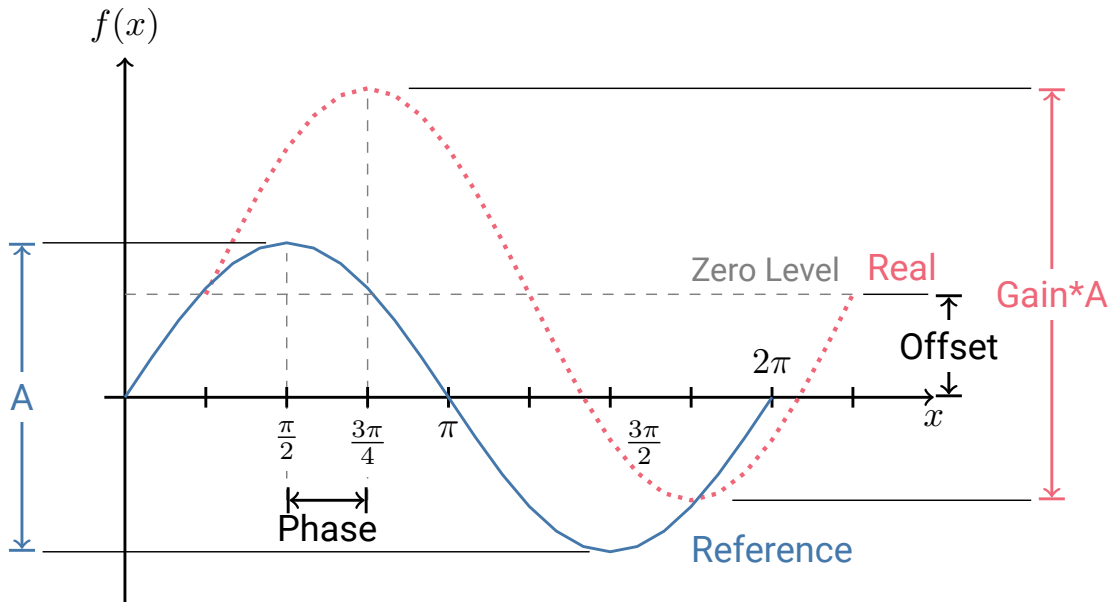
FIGURE 4.1: Graphical representation of the Offset, Gain and Phase (OGP) parameters that can be adjusted to achieve the alignment of the cores. The continuous blue sine wave represents the reference signal. The dotted cyan sine wave represents the samples acquired by the ADC.

two interleaved cores, one core has an inverted clock, which results in two samples per clock cycle, in other words, a higher sampling rate. Although this is a great way to achieve higher rates, it introduces misalignments due to manufacturing variation which can produce an overall degraded performance and spurs in the output spectrum (Jiang et al., 2014). Fortunately, the ADC chip has 12 8-bit Digital to Analog Converters (DACs) that are read and written by its own registry accessed by SPI. Each of the DAC corresponds to an adjustment of one parameter per core (E2V, 2016). These parameters are the OGP. In Figure 4.1, you can see a graphical representation of these parameters by comparing an acquire signal and a reference signal. The Offset can be illustrated as the difference between the signal's zero level and the reference zero level. The Offset can be adjusted in a range of ± 50 mV. The Gain is proportional to the signal amplitude and can be adjusted in a range of ± 18 %. The Phase is a time difference in the sample intervals which can be adjusted in a range of ± 14 ps. The overall transfer function of the output of the ADC is given by

$$output = offset + (input \times gain)$$

Each core can be tweaked in the same way to adjust the acquired signal to the reference signal. The reference signal can be a known input signal or the signal of one of the cores.
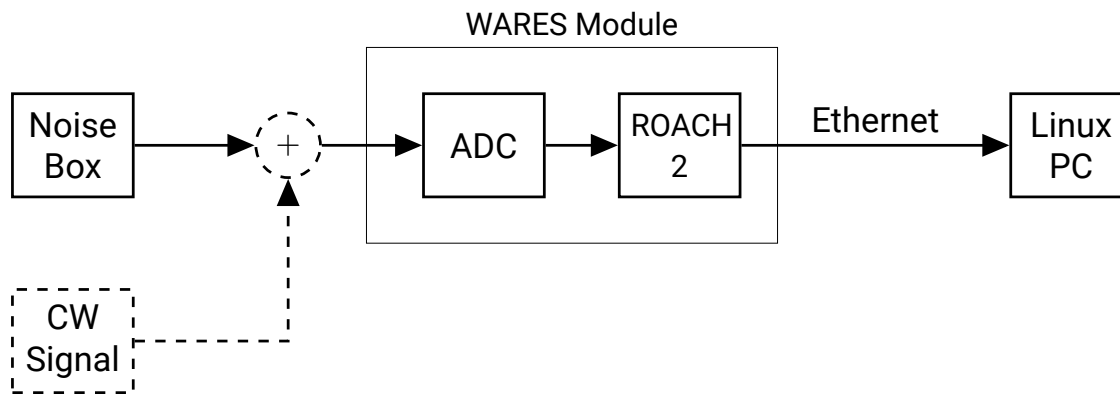
FIGURE 4.2: Block diagram of lab setup. The dashed components were only used for the tests that needed a tone.

Lab Setup

Figure 4.2 shows a block diagram of the lab setup implemented for these tests. The noise box is 1 GHz white Gaussian noise box. It has an attenuation setting that can be adjusted from 0 dBm to -40 dBm. A synthesizer is also used to produce a CW signal. When calculating the full OGP, a 2-way equal splitter is used to input the same signal to the 2 inputs of the ADC. The ADC card and ROACH 2 Board are the same used as a WARES Module. The Linux PC doesn't need any specific characteristics other than having the Corr libraries installed.

Methodology

To determine the values of the OGP, we followed two methods, both based in Patel et al., 2014. These methods are programmed and incorporated in a Python class called ADC_tools. The FPGA design for this test needs to have an ADC block connected to a Snap block therefore the snap block was included in the spectrometer FPGA designs.

The first method acquires data samples from all cores and then fits a sine wave to each core. The OGP are defined as the difference between this sine wave and the reference wave. To implement this method, a mixer is used to add up the noise source with a known single tone signal. The known single tone signal is produced by a synthesizer. The tone selected is a CW sine wave of 800 MHz. However, at the LMT facilities, we won't have one available. Therefore, the second method is more appropriate for actual calibrations on site.

The second method is to use the noise box by itself. The noise box produces Gaussian noise in a band of 1 GHz. Since it is Gaussian noise, the sampled data should also have a Gaussian form. This Gaussian is fitted and the Gaussian parameters are converted to the OGP.

FIGURE 4.3: Plots that show the spectrum before and after the OGP calibration with the 2 methods: tone calibration and noise calibration.

Results

The results are shown in Figure 4.3. Note that the results before and after the OGP are not noticeable. Our conclusion is that on the previous papers where the OGP calibration shows a significant improvement is due because all four core were being calibrated since they were using the single input mode. In our case, the dual input mode, where we only use two cores per input, is being used. The misalignment of these cores is not critical. Nevertheless, the tests for SINAD, SFDR, and SNR (see Section 4.1.2 are more conclusive in showing an actual improvement of the signal after OGP calibration.

4.1.2   SFDR, SINAD and ENOB

This section describes the procedures for determining the Spurious-Free Dynamic Range (SFDR), SIgnal to Noise And Distortion ratio (SINAD) and ENOB of the ADC. These parameters are to be critical for the characterization of an ADC when used in applications for spectrum analyzers (IEEE-Std.1241, 2010).

The SFDR is defined by IEEE-Std.1241, 2010 as the ratio of the amplitude of the ADC's output averaged spectral component at the input frequency to the amplitude of the maximum, or largest, harmonic or spurious spectral component observed over the full Nyquist band for a pure sine wave input of specified amplitude and frequency. It is described by 4.1 and represents the dynamic range of which the smallest signal can be distinguished from a spur (Kester, 2009a).

$$SFDR(dB) = 20log_{10}(\frac{|X_{avm}(f_i)|}{max\{|X(f_H)| \text{or} |X(f_s)|\}}) \tag{4.1}$$

where: X_{avm} $=$ is the averaged spectrum of the ADC output given by Equation (4.2)
f_i $=$ is the input signal frequency
$f_H and f_s =$ are the frequencies of the set of harmonic and spurious spectral components

$$X_{avm}[M] = \frac{1}{K}\sum_{k=1}^{K}|X_k[m]|, m = 0, 1, 2, ..., M - 1 \tag{4.2}$$

where: $K =$ number of data sets
$M =$ the number of samples

The SINAD is defined by IEEE-Std.1241, 2010 as the ratio of the root-mean-square (RMS) amplitude of the analog-to-digital converter output signal to the RMS amplitude of the output noise for a pure sine-wave input. For this case, the noise includes random errors, nonlinear distortion, and effects of sampling time errors. In other words, the noise includes harmonics and all other spectral components other than the signal input and the DC level. It is described by 4.3 and it is considered to be a good indication of the overall dynamic performance of the ADC (Kester, 2009a).

$$SINAD = \frac{A_{rms}}{NAD} \tag{4.3}$$

where: A_{rms} = rms of the signal amplitude and is given by Equation (4.4)

NAD = rms of noise and is given by 4.5

$$A_{rms} = \frac{SineWavePeakAmplitude}{\sqrt{2}} \tag{4.4}$$

$$NAD = \sqrt{\frac{1}{M} \sum_{n=1}^{M} (x[n] - x'[n])^2} \tag{4.5}$$

where: $x[n]$ = the sample data set

$x'[n]$ = the data set of the best-fit sine wave

M = the number of samples in the record

4.4 shows a graphical interpretation of the SINAD and SFDR from a point view of the frequency domain. This also illustrates the procedure followed when measuring these parameters.

The ENOB is calculated from the SINAD by using 4.6.[1] This equation is based from the one of the theoretical Signal to Noise Ratio (SNR) of an ideal N-bit ADC, by changing SNR for SINAD. The ENOB shows the actual bit resolution since there is no perfect instrument (NI, 2017).

$$ENOB = \frac{SINAD - 1.76dB}{6.02} \tag{4.6}$$

Lab Setup

These tests use a lab setup similar to the ADC calibration shown in Figure 4.2, except for the Noise Box. The synthesizer is connected directly to an ADC input.

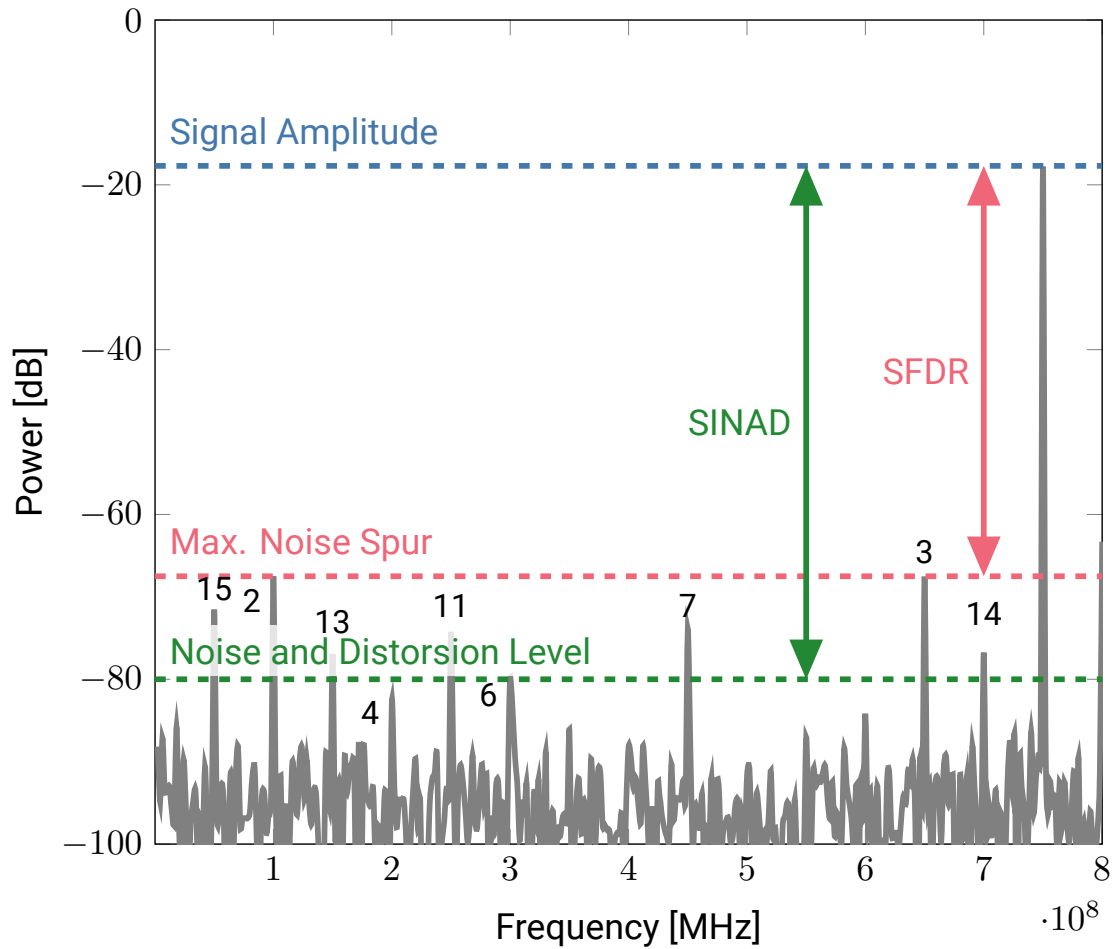
[1]For a derivation, consult (Kester, 2009b; Man, 2012)

FIGURE 4.4: Graphical representation for understanding SFDR and SINAD from a PSD. The plot was made by using a Frequency input of 750 MHz with amplitude 5 mVpp and attenuation of -5 dB. The peak number reference the nth harmonic of the signal. Image inspired by NI, 2017.

Methodology

Our methodology follows the procedure stated in (IEEE-Std.1241, 2010).

Both measurements used the same input frequencies. These were selected to follow the coherent sampling test, which states that the bin number of the applied signal is an exact number. In others, the input frequency needs to have an integer number of cycles within our samples. This can be calculated by using

$$cycles = \frac{f_{input}}{f_s/samples} \tag{4.7}$$

Using the previous criterion, the input frequencies selected are $125, 250, 375, 500, 750$ MHz. These frequencies had a power level of -5 dB to optimize the full scale without clipping the signal. This value was determined by looking at the raw samples from a snapshot.

The IEEE standard defines two methods for calculating SINAD. One method is to fit a sine wave to the raw data, compute the NAD using Equation (4.5) and the SINAD with Equation (4.3). This method is later referred to as the *sin fit* method.

The other method calculates the PSD of the raw data, measures the power of the signal frequency, measures the total power excluding the DC level, and calculates the SINAD by using Equation (4.8). This method is later referred as the *PSD* method.

$$SINAD = 10log_{10}\left(\frac{P_{sig}}{P_{total} - Psignal}\right) \tag{4.8}$$

The SFDR procedure is similar to the SINAD measured by the PSD method but instead of measuring the total power, it measures the sum of the power of the spurs. The SFDR is calculated by using the equivalent of Equation (4.1) in power. [2] This method is also refer as *PSD* method.

We wrote Python scripts that measure SINAD and SFDR by using the methods described previously. These were incorporated in our WARES class. These methods were cycled through the frequencies previously defined and as a result, we have one value per method per input frequency.

Results

The results for SINAD, SFDR and ENOB are shown in Figure 4.5. The SINAD plot compares the values obtained by the PSD method and the sine wave method showing similar values. Each value is the average value obtained from 10 individual snapshots made in a span of 10 min. This plot

---

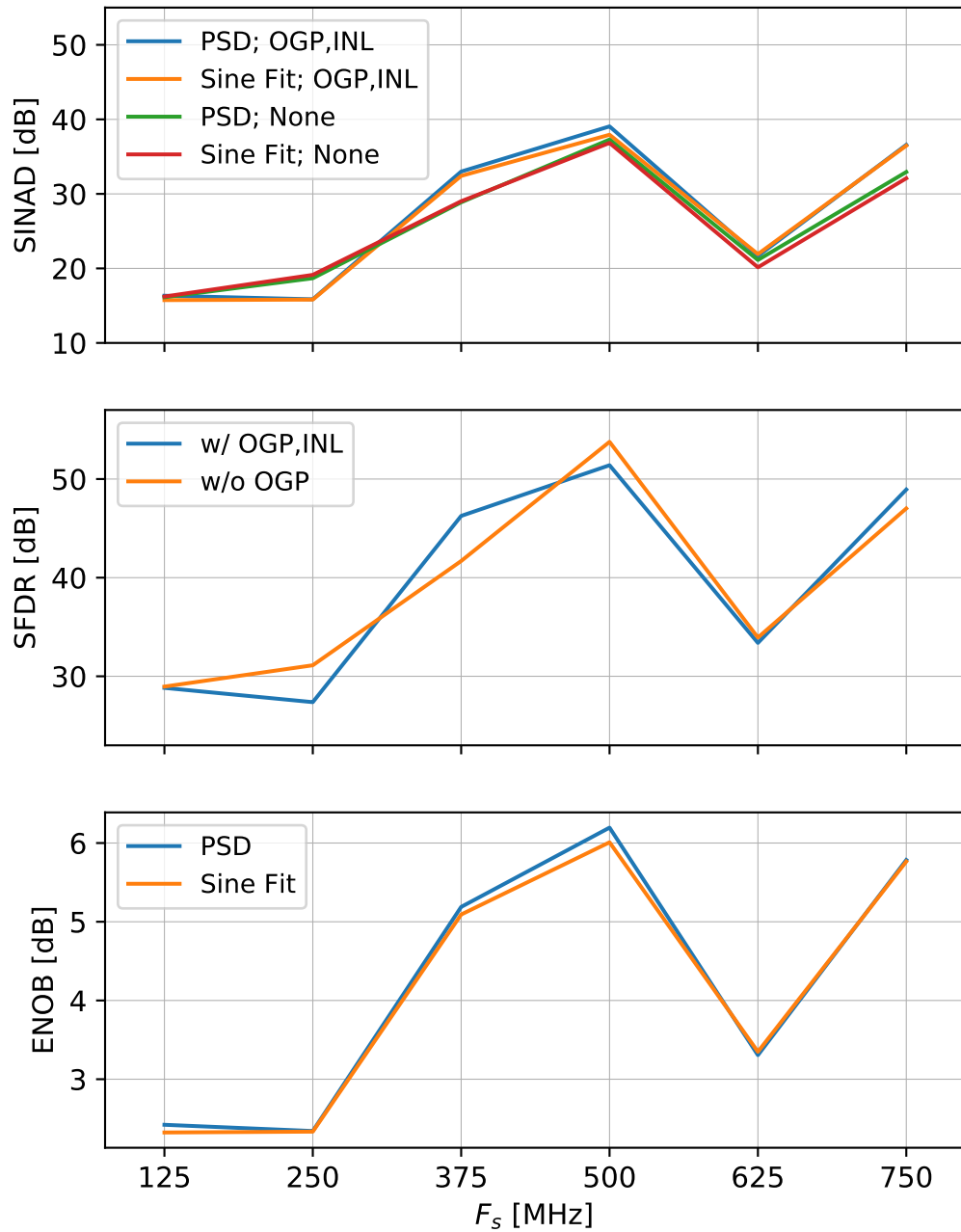[2]Equivalent form is $SFDR = 10log_{10}(P_s/P_{spur})$

FIGURE 4.5:   ADC SINAD and SFDR Results by using frequency input at 125,250,375,500,625,750 MHz with attenuation of -5dB using methods specified in IEEE-Std.1241, 2010.

shows that the methods are consistent and there is no preference from one method to the other. It's also worth noting from these results that the OGP calibration doesn't improve these parameters in contrast with the results from Patel et al., 2014; Jiang et al., 2014.

The SFDR plot compares the values obtained before and after the OGP calibration. Once again, this result shows that the OGP calibration doesn't improve our measurements in any significant way. The best SFDR value is $> 50dB$ while the worst value is $< 30dB$. This represents a dynamic range of the ADC of $\approx 20dB$. These values are lower than the ones showed in fig.7-8 of the datasheet. This difference can be due to the fact that in our application a lower sampling frequency and dual input mode are used.

The overall trend is that the best values for SINAD and SFDR are located in the middle of the band which is the area for the expected results.

The ENOB plot compares the result calculated from the SINAD with OGP parameters. The ENOB varies from ≈ 2 up to 6.

4.2   Linear Range

Every system has a range where its response is linear. This linear response is the range where we can be sure that a 1dB difference in our signal is in fact 1dB. Therefore, our linearity test takes the spectrum of our signal at different power levels and compares it to the real level measured by a power meter. Note that the power meter measures the integrated power of the signal while our spectrum is only in a set bandwidth of 800 MHz. Consequently, our integrated power measured won't be the exactly the same as the mean power of our spectra. Nevertheless, we can note the linear range by a constant slope in our plots.

Lab Setup

The lab setup for the linearity test is similar to the one used for the OGP calibration and is depicted in 4.6. The main difference is that the power meter is used to measure the integrated power of the output of the noise box.

Methodology

The noise box's attenuation setting is used to change the power level of the input. First, we measured the integrated power of the noise box with a 1GHz low-pass filter and the power meter. Then, the output of the noise Box is connected to the ADC input. The 800 MHz FPGA design is loaded and
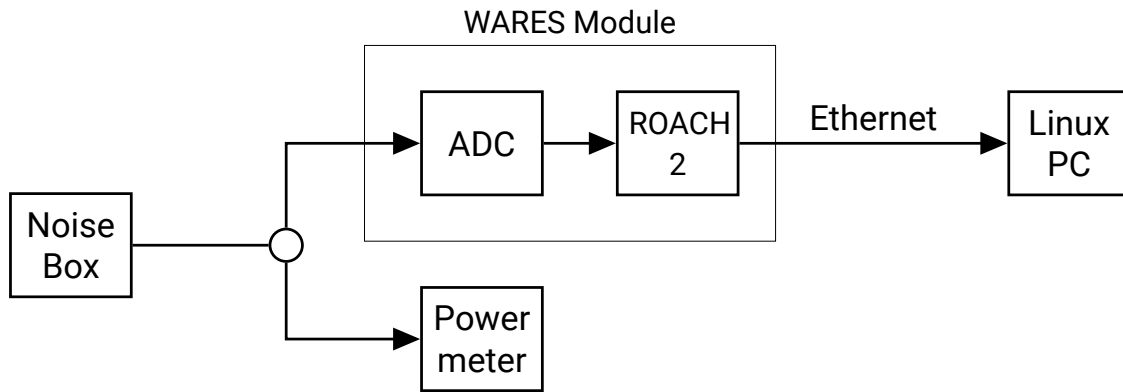
FIGURE 4.6: Lab setup for Linearity Test.

the spectrum of the signal is taken at different power levels. Using Python, the mean power of the spectra is calculated for each power level and finally saved it into an array. Finally, the integrated power vs the mean power of the spectra.

Additionally, a single measurement was done at different quantization gain and sync scale values to show the effect of these in the linear range. To do so, the previous steps were repeated with the new parameters under test. The gain is set as a value in hexadecimal form while the scale is a power of two number. The default scale and gain were 1024 and 0xFFFFFF, respectively.

Results

As seen in Figure 4.7, changing the parameters of scale and quantization gain affect the linear range. The gain parameter We concluded that the optimal setting is a scale of 1024 and a quantization gain of 0xFFFFF.

4.3   Allan Variance

A common practice for increasing the SNR is to integrate for long periods of time. This practice is valid until a certain amount of time at which the SNR starts to worsen. This effect is because at short integration times the random noise dominates the signal but at long integration times, the drift noise starts to have a dominant contribution, consequently, worsening the SNR (Bussa, 2011). The Allan variance plot is a common tool that allows us to calculate the maximum integration time at which we can get optimal results without the observations being affected by the drift noise.

The Allan variance can be defined as the ordinary statistical variance of the difference of two contiguous measurements (Schieder and Kramer, 2001). These two contiguous measurements are
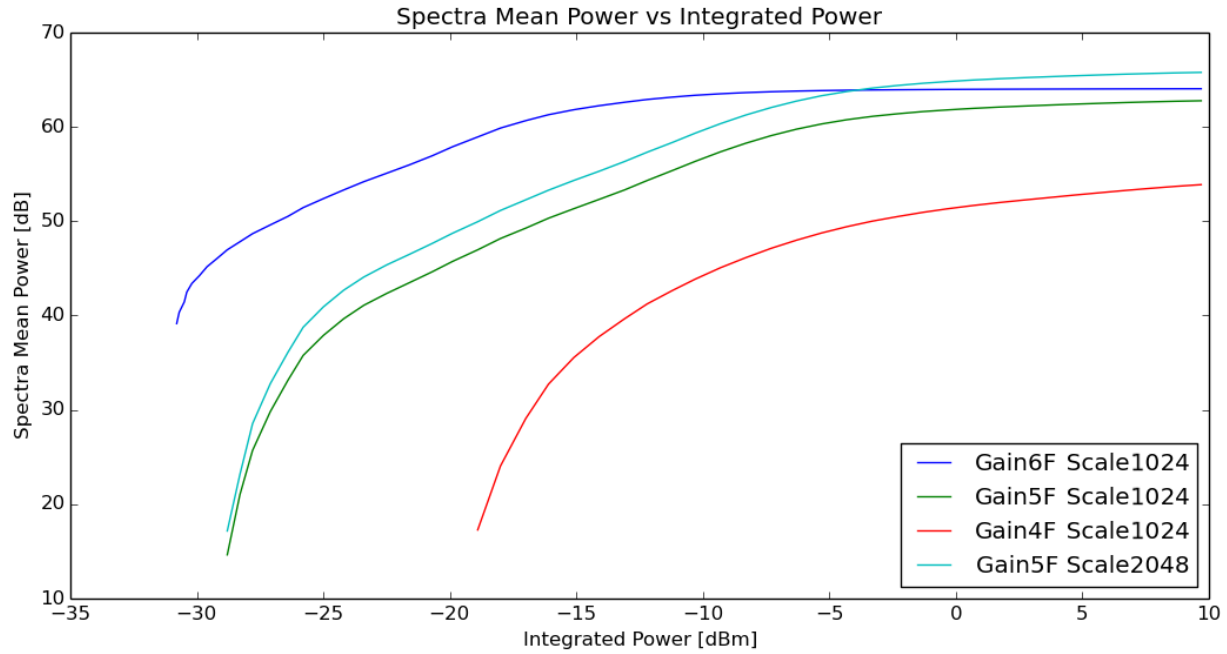
FIGURE 4.7: Plot for linearity test with different values of scale and quantization gain. The best linear range was 20dB with quantization gain of 0xFFFFFF and scale of 1024.

samples taken without any dead time in between. The ideal Allan curve is calculated from the radiometer equation, expressed in 4.9.

$$\sigma_{ideal} = \frac{\sqrt{2}}{\sqrt{f_o \tau}} \tag{4.9}$$

This method is used to detect long variations in our data. The time at which the Allan variance is the minimum is called the Allan time and is used to set the maximum integration time for an observation.

Lab Setup

The lab setup is the same as the one used for the linearity test, shown in Figure 4.6. The output of the noise source is connected to an input of the ADC. Then, the signal is processed by the ROACH 2 board and the data is acquired through an Ethernet connection.

Methodology

The output of the noise box is set with an attenuation of 0dBm. Then, we connect it to an ADC input. The 800 MHz design is loaded into the FPGA using the optimum settings obtained from the previous tests.

Then, a Python script, which takes a specified number of spectra continuously, is started, The number specified was 50000 spectra. The spectra are saved into a file for future analysis. This step takes about 2 to 3 hours per pixel or output.

After the acquisition is complete, another Python script is started. This script calculates the Allan variance for an specific equivalent integration time. At first, an equivalent time of $\tau$is assumed and its value is the average of the time taken to obtain one spectrum. Then, two continuous spectra are normalized by $\frac{ON-OFF}{OFF}$.[3]After all spectra are normalized, the mean and variance of a specific section of the spectra are calculated. In our case, the selected spectra section is from frequency bin 500 to 1000. The variance calculated is the Allan variance for a τintegration time.

The steps are repeated but for an equivalent integration time of 2τ, then $3\tau$and so on. Figure 4.8 shows in a graphical for how the spectra with an equivalent integration time n$\tau$is done. The steps are repeated until at least two $ON - OFF$ pair with equivalent time $N/4$ is possible, where N is the number of samples taken.

Finally, the calculated Allan variance values are plotted on a log scale with respect the log of the equivalent integration time.

$$\sigma^2 = \frac{\sum(X - \mu^2)}{N} \tag{4.10}$$

Results

In 4.9, is the plot for the Allan variance. The Allan time is $\approx 10^2$ seconds.

---

[3]The ON spectrum is the equivalent of a signal spectrum while the OFF spectrum is for a reference spectrum. This practice is common for radio observations.
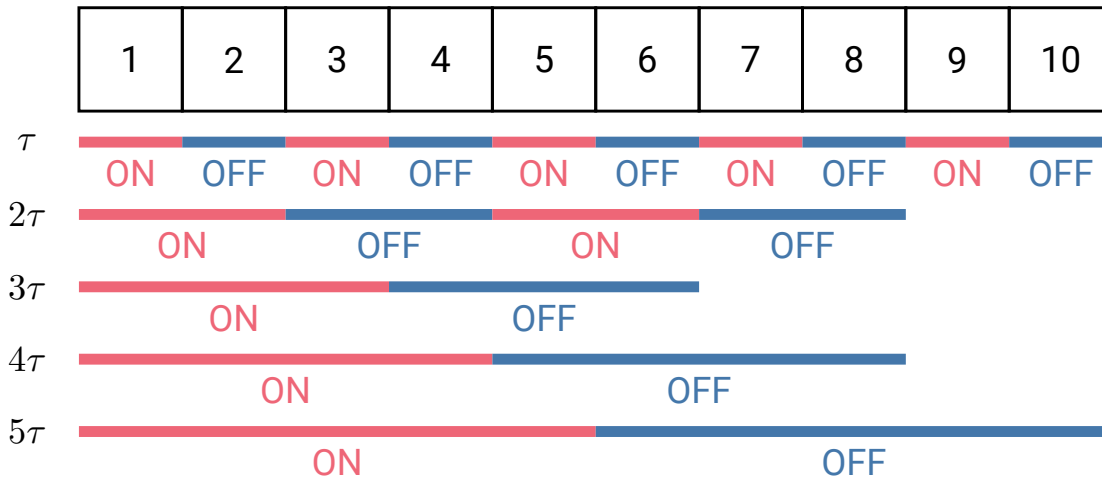
FIGURE 4.8: A graphical explanation for calculating the Allan Variance from continuous observations with a set integration time. The numbered squares represent spectrum taken without dead time in between. Each spectrum has an integration time of τ. Therefore, the first Allan variance calculated is with the data that have $T_{int} = \tau$. Then for the second Allan variance, we calculate the average of both samples needed for having a $T_{int} = 2\tau$. And so on, until we no longer have an ON and OFF spectra pair or until we get our maximum desired integration time.
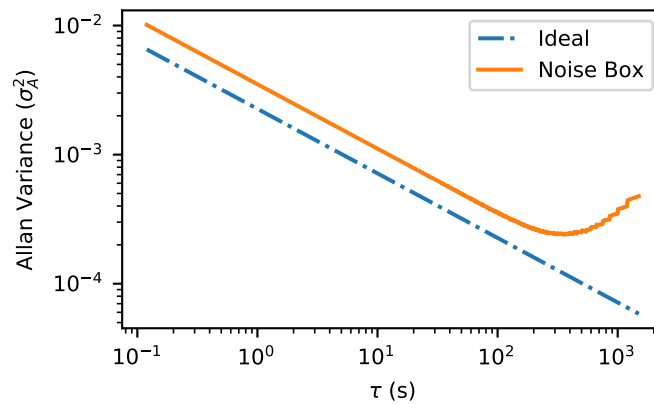
FIGURE 4.9: Allan variance plot using a 1GHz Noisebox and WARES module. The spectra used was obtained using the 800 MHz FPGA design and frequency bins 500-1000. This plot shows an Allan time of ≈ 100 seconds.

Chapter 5

WARES and SEQUOIA

This chapter will describe the procedure to other tests involved in the characterization of SEQUOIA and WARES. Another test is the process we followed to determine the noise temperature of the system using the method of Y-factor in Section 5.1. Finally, the stability test results for the full system in Section 5.2.

5.1   Receiver Temperature

The receiver temperature is a parameter that describes the sensitivity of our instrument. Hence, the importance of calculating it. Furthermore, it is a contribution that affects the system temperature as it is composed of several contributions such as the sky, spillover radiation, galactic background, and many others.

A method for measuring the receiver temperature is by calculating the Y-factor. The Y-factor is the ratio of two power levels, one in the noise source on and the other with the noise source off.

The power level is proportional to noise temperature.

This receiver temperature is defined as the temperature a resistor would be if it has the same power as the receiver noise temperature. The system noise temperature is composed of the receiver's and antenna's inherent noise temperatures: $T_{sys} = T_{rx} + T_A$.

The receiver temperature is a very important characteristic that we need to measure for our system.

The receive temperature measurement will be done through every step of the SEQUOIA system all the way to a WARES module.

$$Y_{factor} = \frac{hot - off}{cold - off} \tag{5.1}$$

TABLE 5.1: Spectrum Analyzer settings used for the verification of SEQUOIA's output

Parameter	Value
Bandwidth	Two-channel − A&C
Video Resolution	ZDOK 0
Bandwidth Resolution	1:1

FIGURE 5.1: Plots of SEQUOIA output from spectrum analyzer

$$T_{noise} = \frac{T_{hot} - T_{cold} * Y_{factor}}{y_{factor} - 1} \tag{5.2}$$

Lab Setup

In front of SEQUOIA, we set up a cold load, which is a Styrofoam bucket filled with liquid nitrogen and some absorbers. The absorbers serve two purposes: one is to make the temperature gradient more even and the second is to fill the volume so less liquid nitrogen is used. Also, we set up a hot load, which is a piston with an absorber material mounted on a metal plate facing SEQUOIA. The temperature of the absorber is ambient temperature, 290K. This piston is controlled by the computer.

For the first step, the output of SEQUOIA was connected to a spectrum analyzer. The spectrum analyzer is controlled from the computer by using GPIB.

For the later steps, the output of SEQUOIA is connected to the IF processors. This will make the signal go through all the system up to a WARES module.

Methodology

The first step is to verify the integrity of SEQUOIA. This is done by looking at SEQUOIA output through a spectrum analyzer. The spectrum analyzer is controlled by the computer via GPIB and python. The setting used on the spectrum analyzer a listed in table **??**. The data displayed on the screen of the spectrum analyzer was acquired and save it in text files. Since the spectrum analyzer only has one input, this procedure had to be repeated for all 16 pixels in both bands of SEQUOIA.

Figure 5.3 shows two full set of measurements. The first measurement, in blue, shows the power of each pixel through both bands. After the first measurement, pixel 7 had an excess of power with respect to all other pixels and with respect to previous years. This behavior through the band pointed out a malfunction at this pixel. This led to stopping the tests for receiver temperature.

The UMass staff had to open SEQUOIA's dewar and dismantle various pixels to be able to get to pixel 7. The affected pixel was repaired and assembled back. Once SEQUOIA was cool again, the procedure was repeated. The second measurement, in red, shows that only pixel 7 had changed. This measurement was compared with measurements of previous years and was determined that the power level was consistent. It was concluded that after the repair, all 16 pixels had a similar behavior as the one measured in 2015.

After the measurements with the spectrum analyzer were done, The outputs of SEQUOIA were connected to the IF processors. The hot load was kept in front of SEQUOIA. As mentioned previously, the IF processors have an internal ADC for monitoring the signal. These ADCs were used to find the optimal attenuation settings for each pixel. A Python script was written that finds the best attenuation by measuring the voltage of the signal. This voltage was set to be $0(2)$V for optimal attenuation. The script starts at a predefined attenuation level and determines whether to lower or increase the attenuation based on the voltage measured. When this process is complete, the optimal attenuation settings are saved into a file from which they can be loaded for later use. These attenuations were done at different frequencies from both bands. It was expected that the attenuation setting will follow the shape of the signal acquired by the spectrum analyzer in the previous steps.

After confirming that every pixel and attenuation was functioning correctly, the noise measurement tests were applied at two different stages of SEQUOIA system: the output of IF processors and the output of WARES.

The noise temperature measurements after the IF processors were done by using the internal ADC with the aid of a python script. The python script measured the signal of the cold load, the hot load and an offset measurement. The offset measurement was done by turning off the second internal amplifier of SEQUOIA which produced a measurement of power without any signal. These 3 measurements are used to calculate the Y_factor and later to calculate the noise temperature of the system with the equations 5.1, 5.2.

Figure 5.4 shows the noise temperature measured at different frequencies for all 16 pixels at the output of the IF processors.

Noise temperature is as expected at each frequency and consistent with previous measurements.

Before calculating the noise temperature at the output of WARES, the power of the signal was measured before connecting it to the WARES module. At this step, it was noted that the power level of signal was too high. The circuit diagram was analyzed and found that the Baseband IF processors included two amplifiers with ≈ 15 dB of gain, which was consistent with the excess power level measured previously. These amplifiers were jumped.

After confirming the signal power was the correct level, the signal was connected to the input of the WARES module. A cold spectra, hot spectra, and an offset were measured. With these, the
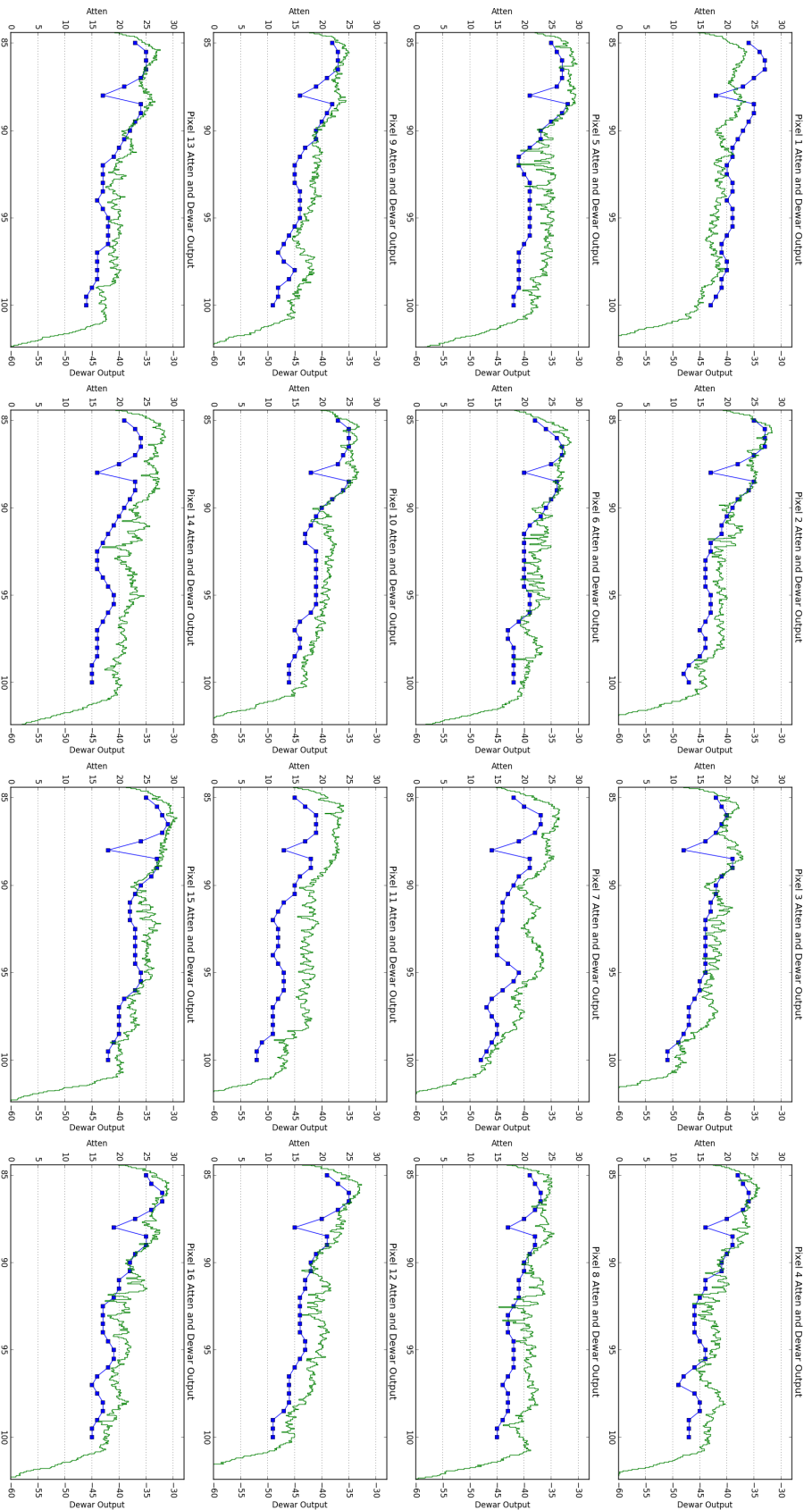
FIGURE 5.2: Plots of SEQUOIA output on the lowband from spectrum analyzer vs attenuation setting from IF processors
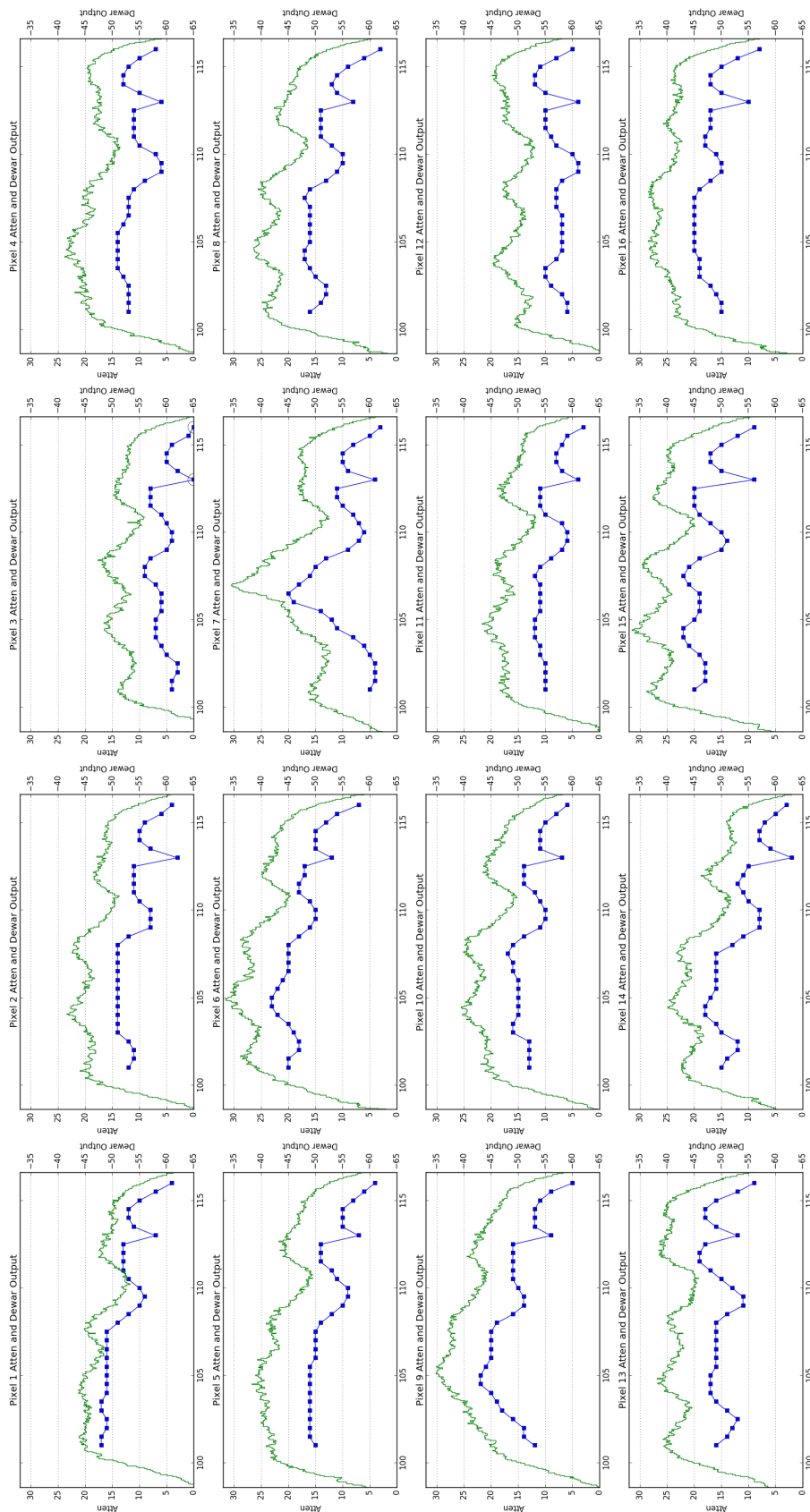
FIGURE 5.3: Plots of SEQUOIA output on the highband from spectrum analyzer vs attenuation setting from IF processors
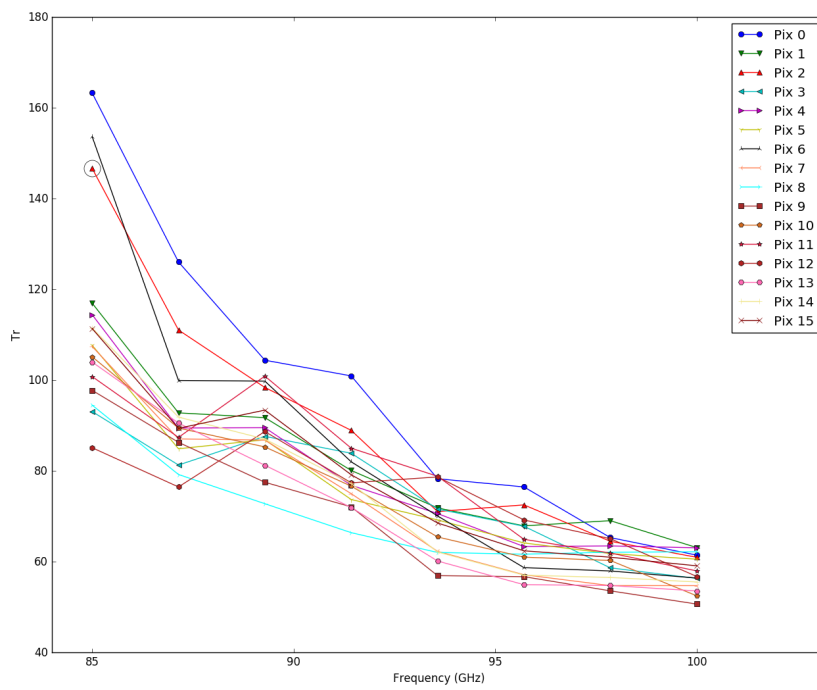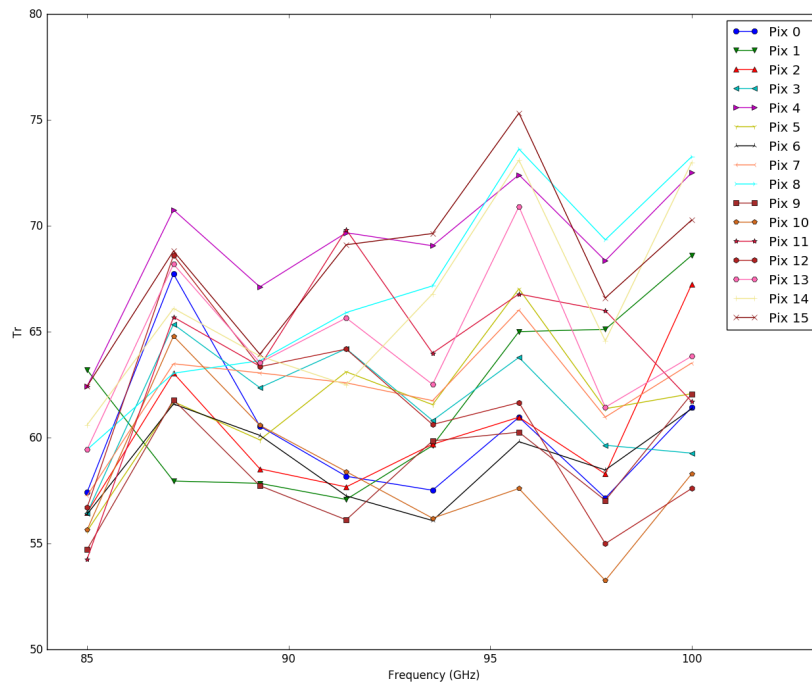
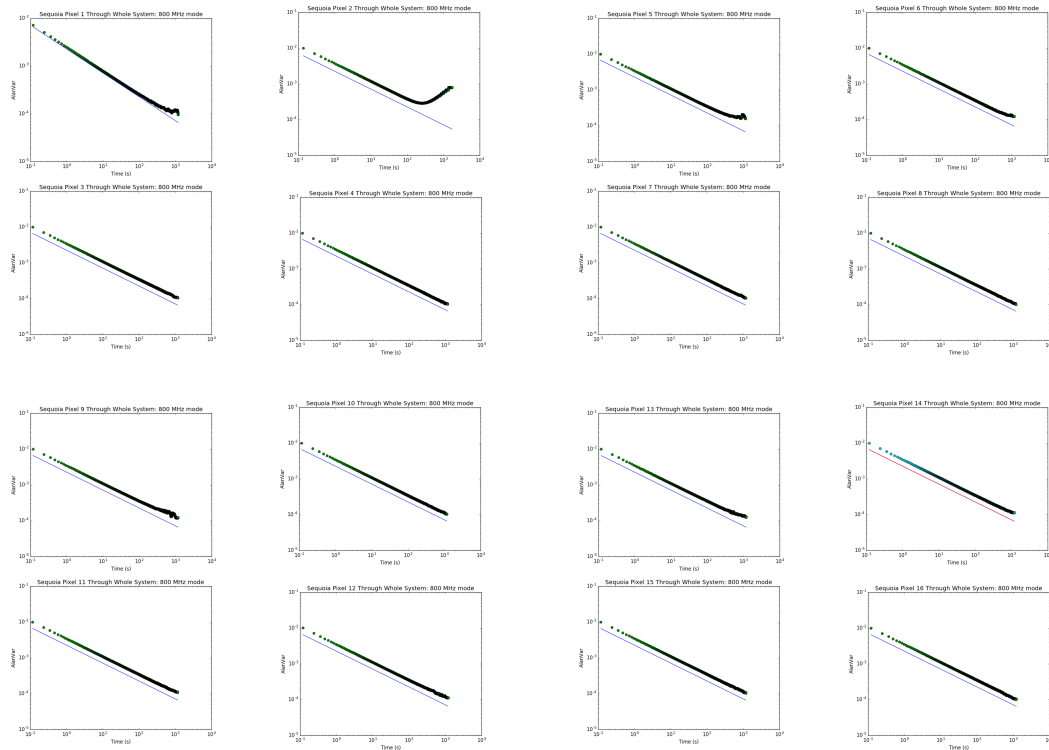FIGURE 5.4: Noise Temperature at IF processors

FIGURE 5.5: Allan Variance for all 16 pixels of SEQUOIA through the whole system.

Y-factor was calculated and so, the receiver temperature using Equation (5.1) and Equation (5.2), respectively.

The receiver temperature was determined to have an average of 77K at low frequencies.

5.2   Allan Variance

The theory of this parameter was explained in 4.3 This section was included in this thesis for documentation. The procedure for this test is similar to the one used in 4.3 except that instead of using a noise source we use the signal from SEQUOIA looking at the hot load. As mention previously, for the writing of this thesis, there was one fully functional WARES module. So the stability test was done by connecting 4 pixels at a time. Figure 5.5 shows the Allan Variance Plot for all pixels using the 800 MHz design.

Chapter 6

Summary and Future Work

6.1 Summary

SEQUOIA is a 16-pixel focal plane array to be installed on LMT by the end of the year. Even though SEQUOIA has already been working at the 14-m FCRAO telescope, it needed a few upgrades before being able to work with the LMT. One of these upgrades is WARES, an FPGA spectrometer design for use with SEQUOIA. WARES is mainly composed of modules that include CASPER's ROACH 2 board and 2 ADC cards.

In Chapter 2, we listed the hardware components used for the ADC clock and the power supply. Also, it shows the enclosure design to fit up to 8 modules. Furthermore, it explained the CASPER tools needed for the FPGA designs and the interface python scripts to send commands such as load up a specific design, setting variables and reading the results. Additionally, it included a section that describes the python class created for interfacing WARES with the LMT.

In Chapter 3, the FPGA design code was explained. The code starts by using the ADC block for acquiring the signal. Then it passes through a PFB filter in preparation for the FFT. The output of the FFT is converted into power. The result is then quantized and accumulated in the BRAMs. The 800MHz design served as the basis for the 400 MHz and 200 MHz designs. In addition, it was showed that the utilization of the Black Box method reduce compilation time and minimized timing errors.

In Chapter 4, the characterization procedure and relevant parameters were explained. It started with the ADC characterization that included an OGP calibration before calculating the SFDR, SINAD, and ENOB. It was shown that the OGP calibration was not very critical for our application. The average results for the 800 MHz bandwidth are $SFDR = 20$, $SINAD =$ and $ENOB = 4$. These were followed by the determination of the linear range which was highly dependent on the quantization gain. The optimal quantization gain was determined to be $0xFFFFF$ giving a linear range of ≈ 20 dB.

Finally, in Chapter 5, the procedure followed to determine the noise temperature was described. During the first step, a malfunction of pixel 7 was noted. This was corrected before continuing the process. On a subsequent step, it was discovered that the gain in the Baseband IF processors was too high for a WARES input. This gain was removed from the PCB boards. Finally, we were able to determine a noise temperature of ≈ 60 K for the low band and ≈ 80 K on the high band. The Allan variance plot was calculated for all pixels which consistently showed an Allan time higher than 100 ms.

6.2   Future Work

There are still several pending tasks before installing SEQUOIA and WARES at the LMT.

On this thesis, it was included some tests made with the 800 MHz design. The evaluation of the parameters discussed in this thesis is still pending for both the 400 MHz and 200 MHz designs. Also, during the elaboration of these tests, we characterized only one WARES module. The rest of the modules are still in process of being purchased or delivered to UMass. Once they have arrived, these tests will be applied to them.

Another pending task is to test the optical mirrors to couple SEQUOIA focal ratio to LMT's. It was designed at least 2 mirrors for this purpose: M6 and M7. These are being tested in UMass at the moment of writing this thesis. A major concern is the development of a system which will facilitate the alignment and the mounting on the LMT. For this purpose, the mirrors have a temporal center hole from which a laser can pass through and be used for alignment. But since the wavelength is different, the path followed by the light is also different. This difference needs to be measured for this method to work. In addition, the beam pattern of the mirrors needs to be characterized to confirm that the beam is focused. The procedure for testing the mirrors is to measure the beam pattern. A noise horn is mounted on top of a line rail and is moved in one direction every set offset through an optical bench. The signal is acquired by the ADC's on the IF processors and read on the computer. The beam pattern for each pixel is made by obtaining the measurements of the different positions of the noise horn. With this information, a Gaussian beam is fitted so we can obtain the FWHM and determined if it is inside tolerance for a focused beam.

Another pending task is to improve the dump rate of the designs. As mentioned in the introduction, SEQUOIA is planned to be used with On-The-Fly mapping, but the maximum permissible dump rate for this application is 100ms with an ideal dump rate being faster than 50ms. Until now, the average dump rate measured with our designs is of 80 ms for single input measurement but 400ms when all 4 inputs are being used. One proposed solution to this problem is the use of UDP transfer. Until now, the design uses a standard Ethernet connection using TC/IP which includes 'handshaking' with each packet sent, adding time to the transfer. Fortunately, the ROACH 2 board includes

an Ethernet connection directly to the FPGA different from the connection used to the Master PC. In other words, we can have an Ethernet connection for sending control commands and another to send the data. Additionally, the transfer time can be optimized by using parallel ports and processors.

An upgraded environmental box needs to be created. An environmental box is a device that reads and monitors the temperature and pressure sensors inside the SEQUOIA dewar. The previous model was proven to produce noise inside the observation band and it needed a person in the same place to monitor it. A new model was proposed which will be based on Raspberry Pi. This technology will make the design portable, flexible and with the ability to connect to the Ethernet network at LMT. This is very important since the values of the sensors can be monitored remotely. A prototype was already made but the PCB design is still pending.

Many of this pending tasks won't affect the delivery of SEQUOIA system to the LMT for installation by the end of this year.

Bibliography

Academies, The National (2015). *Handbook of Frequency Allocations and Spectrum Protection for Scientific Uses: Second Edition*. NATL ACADEMY PR. 280 pp. ISBN: 0309376599.

Bussa, Srikanth (2011). "A FPGA base Spectral Line and Pulsar Observing System for RadioAstronomy". MA thesis. The University of Akron.

Condon, James J. and Scott M. Ransom (2015.). *Lecture notes in Essential Radio Astronomy*. NRAO. URL: http://www.cv.nrao.edu/~sransom/web/xxx.html.

E2V, Technologies, ed. (2016). *Quad ADC*. EV8AQ160. Datasheet 0846J BDC 03 16. URL: http://casper.berkeley.edu/wiki/images/1/19/Ev8aq160.pdf.

Estalella, Robert and Guillem Anglada (1999). *Introducción a la Física del Medio Interestelar*. 50th ed. ISBN: 84-8338-098-6. URL: http://www.am.ub.edu/~robert/ifmi/ifmi.pdf.

Ferrusca, Daniel (2006). "A Cryogenic He bolometer System for Detecting (sub)millimeter Wavelength Radiation". PhD thesis. INAOE.

Goldsmith, Paul F. et al. (2008). "Large−Scale Structure of the Molecular Gas in Taurus Revealed by High Linear Dynamic Range Spectral Line Mapping". In: *The Astrophysical Journal* 680.1, p. 428. DOI: 10.1086/587166. URL: http://stacks.iop.org/0004-637X/680/i=1/a=428.

Henry Chen, Peter McMahon and Aaron Parsons (2008). *Sync Pulse Usage in CASPER DSP Blocks*. URL: https://casper.berkeley.edu/memos/sync_memo_v1.pdf.

Hickish, Jack et al. (2016). "A Decade of Developing Radio-Astronomy Instrumentation using CASPER Open-Source Technology". In: *Journal of Astronomical Instrumentation* 05.04, p. 1641001. DOI: 10.1142/s2251171716410014. URL: http://www.worldscientific.com/doi/abs/10.1142/S2251171716410014.

IEEE-Std.1241 (2010). *IEEE Standard for Terminology and Test Methods for Analog-to-Digital Converters*.

INAOE (2016). *LMT- Large Millimeter Telescope Alfonso Serrano*. (Accessed on 11/14/2016). URL: http://www.lmtgtm.org/.

Jiang, Homin et al. (2014). "A 5 Giga Samples Per Second 8-Bit Analog to Digital Printed Circuit Board for Radio Astronomy". In: *Publications of the Astronomical Society of the Pacific* 126.942, p. 761. URL: http://www.jstor.org/stable/10.1086/677799.

Kennicutt, Robert C. and Neal J. Evans (2012). "Star Formation in the Milky Way and Nearby Galaxies". In: *Annual Review of Astronomy and Astrophysics* 50.1, pp. 531−608. DOI: 10.1146/annurev-astro-081811-125610.

Kester, Walt (2009a). *Understand SINAD, ENOB, SNR, THD, THD + N, and SFDR so You Don't Get Lost in the Noise Floor*. Tech. rep. Version A. Analog Devices, p. 8. URL: http://www.analog.com/media/en/training-seminars/tutorials/MT-003.pdf (visited on 09/10/2017).

Kester, Walter (2009b). *Taking the Mystery out of the Infamous Formula, "SNR = 6.02N + 1.76dB," and Why You Should Care*. Tech. rep. Version A. Analog Devices. URL: http://www.analog.com/media/en/training-seminars/tutorials/MT-001.pdf (visited on 09/11/2017).

MacMahon, David (2010). *Optimize CASPER Development by "Black Boxing" Designs*. URL: https://casper.berkeley.edu/wiki/images/a/a4/Black_box_memo.pdf.

Man, Ching (2012). *Quantization Noise: An Expanded Derivation of the Equation, SNR = 6.02 N + 1.76 dB*. Tech. rep. MT229. Analog Devices, p. 4. URL: http://www.analog.com/media/en/training-seminars/tutorials/MT-229.pdf (visited on 09/11/2017).

Narayanan, Gopal, Ronald Snell, and Ashley Bemis (2012). "Molecular outflows identified in the FCRAO CO survey of the Taurus Molecular Cloud". In: *Monthly Notices of the Royal Astronomical Society* 425.4, pp. 2641–2667. DOI: 10.1111/j.1365-2966.2012.21579.x. URL: http://dx.doi.org/10.1111/j.1365-2966.2012.21579.x.

Narayanan, Gopal et al. (2008). "The Five College Radio Astronomy Observatory CO Mapping Survey of the Taurus Molecular Cloud". In: *The Astrophysical Journal Supplement Series* 177.1, p. 341. URL: http://stacks.iop.org/0067-0049/177/i=1/a=341.

NI (2016). *Block RAM (BRAM) on an FPGA. LabVIEW Communications System Design Suite 2.0*. National Instruments. URL: http://www.ni.com/documentation/en/labview-comms/2.0/fpga-targets/block-memory/.

– (2017). *White paper: Understanding Frequency Performance Specifications*. Tech. rep. National Instruments. URL: http://www.ni.com/white-paper/3359/en/.

Patel, NA et al. (2014). "Characterizing the Performance of a High-Speed ADC for the SMA Digital Backend". In: *Journal of Astronomical Instrumentation* 3.01, p. 1450001. URL: http://www.worldscientific.com/doi/pdf/10.1142/S2251171714500019.

Payne, John M. (1989). "Millimeter and Submillimeter Wavelength Radio Astronomy". In: *Proceedings of the IEEE* 77.7, pp. 993–1017. DOI: 10.1109/5.30751.

Price, Danny C. (2016). "Spectrometers and Polyphase Filterbanks in Radio Astronomy". In: *to be published in the WSPC Handbook of Astronomical Instrumentation* 1. URL: http://arxiv.org/abs/1607.03579.

Remijan, A.J. (2010). *Splatalogue Database for Astronomical Spectroscopy: Splatalogue Quickstart Guide*. National Radio Astronomy Observatory. URL: https://books.google.com.mx/books?id=Z51jtwAACAAJ.

Schieder, R. and C. Kramer (2001). "Optimization of heterodyne observations using Allan variance measurements". In: *Astronomy & Astrophysics* 373.2, p. 746. DOI: https://doi.org/10.1051/0004-6361:20010611.

SEQUOIA (2017). *Millimeter Laboratory*. (Accessed on 11/16/2016). University of Massachusetts. URL: https://www.astro.umass.edu/fcrao/instrumentation/sequoia/seq5.html.

Stojimirović, Irena, Gopal Narayanan, and Ronald L. Snell (2007). "Discovery of a Molecular Outflow in the Haro 6-10 Star-forming Region". In: *The Astrophysical Journal* 660.1, p. 418. URL: http://stacks.iop.org/0004-637X/660/i=1/a=418.

Wall, W. F. et al. (1999). *Millimeter-Wave Astronomy: Molecular Chemistry & Physics in Space*. Ed. by W. F. Wall et al. Springer Netherlands. DOI: 10.1007/978-94-011-4714-9.

Wilson, Thomas L. (2009). "Introduction to Millimeter/Sub-Millimeter Astronomy". URL: https://arxiv.org/abs/0903.0562.

Wilson, Thomas L., Kristen Rohlfs, and Susanne Hüttemeister (2013). *Tools of Radio Astronomy*. Sixth Edition. Springer Berlin Heidelberg. DOI: 10.1007/978-3-642-39950-3.

Xilinx (2013). *EDK Concepts, Tools, and Techniques*. URL: https://www.xilinx.com/support/documentation/sw_manuals/xilinx14_7/edk_ctt.pdf.

Yamamoto, Satoshi (2017). *Introduction to Astrochemistry. Chemical Evolution from Interstellar Clouds to Star and Planet Formation*. Springer Japan. ISBN: 978-4-431-54171-4. DOI: 10.1007/978-4-431-54171-4. URL: http://www.ebook.de/de/product/28543836/satoshi_yamamoto_introduction_to_astrochemistry.html.

Zeballos, M. et al. (2016). "Reporting the first 3 years of 225-GHz opacity measurements at the site of the Large Millimeter Telescope Alfonso Serrano". In: ed. by Helen J. Hall, Roberto Gilmozzi, and Heather K. Marshall. DOI: 10.1117/12.2232168.

List of Acronyms